Two-Dimensional Magnetic Micro-Module Reconfigurations Based on Inter-Modular Interactions

Shuhei Miyashita*, Eric Diller, and Metin Sitti
NanoRobotics Lab., Department of Mechanical Engineering, Carnegie Mellon University
5000 Forbes Ave, Hamerschlag Hall D308, Pittsburgh, PA 15213
+1 617-253-6532, shuheim@csail.mit.edu

Abstract

We present a scheme of two-dimensional module reconfiguration based on interactions between microscale magnetic modules with potential applications in micro-robotics, particularly in automatic micro-fabrication, non-invasive diagnoses, micro-surgery, and drug delivery at unreachable sites. The approach taken is a mixture of a top-down engineering approach and a bottom-up self-assembly approach, where reconfiguration commands are delivered from outside the workspace in the form of a magnetic field, which directs configuration changes in the set of modules by changing the strengths of individual magnetic moments. The magnetic modules in the study, 750 μm in size, are constrained to a liquid surface, providing a simplified two degrees of freedom translational motion environment, where the laterally interacting inter-module magnetic force determines the assembly configuration. In this way, the relative distance of the magnets simply reflects the strength of the interactions, and thus easily enables the design of the system's reconfiguration scenario. Reconfiguration occurs when the magnetic attractive forces are changed. To direct the assembly morphology in a controlled manner, the modules are addressed magnetically by incorporating a different magnetic material into each module type, each with different magnetic hysteresis characteristics. For addressing different modules' magnetizations, we incorporate three different magnetic materials that feature different magnetic coercivities. This allows for the independent control of the magnetization of each material using applied external fields of varying strength, leading to arbitrary configuration change in a three-module set and limited control over a four-module set. General cases with more than five modules are further discussed.

keywords
Reconfigurable micro-robots, inter-module interactions, remotely reversible magnetic moment, addressability, micro self-assembly.

1 Introduction

Increased demand for fabrication of complex micro-structures below sub-mm scale has recently led researchers to confront the problem of how to handle multiple micro-components for efficient synthesis. Such technology can potentially be used at unreachable sites for non-invasive diagnoses,

*Shuhei Miyashita is currently with Computer Science and Artificial Intelligence Laboratory, Massachusetts Institute of Technology. 32 Vassar Street, Cambridge, MA, 02139.

micro-surgery, and drug delivery inside the human body; the micro-devices could be injected and delivered, at which point they would self-assemble and self-reconfigure for expected tasks (Sitti 2009). Micro-robotic exploration now focuses on the possibility of smaller, more autonomous devices that can function at unreachable sites, such as the esophagus, the blood vessels, and the eye (Kummer et al. 2010). As addressed by Gendreau et al. (2010), one of the scoped features of micro-assembly and micro-reconfiguration would be an *automatic assembly* method, which would eventually be followed by the realization of *automatic microfactory*. Toward this end, as the assembly processes become more complex and are held at more inaccessible sites, remotely and coordinately operating micro-component transformations becomes crucial. One focus has therefore been to investigate ways to independently handle multiple micro-modules that attribute unlimited degrees of freedom, and to manage trustful assembly.

In artificial self-assembly systems, consisting of a countable number of components, there are two known issues to be taken into account: how to avoid *assembly connection error* and *assembly sequence error*. In self-assembly, an undesired components' attachment is induced, mainly due to the low addressing capability, to attain the adequate bonding affinity level for connections. Insights from molecular biology remind us of the importance of the fertile addressing capability in minimizing assembly errors (or undesired attachment), which is induced mainly due to the low addressing capability, to attain the adequate bonding affinity level for connections. Protein's trick of distributing bonding sites around the body, and changing the morphology to pose as another bonding site, reminds us of the importance of internal states, which enables the component to feature different properties. It exploits non-covalent bonds (hydrogen bonds, ionic bonds, and van der Waals attractions) as interaction forces and somehow achieves a remarkable specificity in docking with other selected molecules. The *assembly sequence error* occurs when components assemble in an undesired sequential order, and hence the targeted structure is therefore unreachable because earlier assembled components block the way. In general, the problem of deriving the final configuration from a given set of components/environments is called the *forward problem* (Pelesko 2007), and it is known as a computationally expensive issue (the game *Tetris*® is known as an NP-hard (Demaine et al. 2002); also, it may be useful to mention that some situations in self-assembly resemble the *Knapsack problem*, which is known as an NP-complete).

1.1 Approaches to Micro-Robot Assembly

Manipulating a specific micro-module, by applying a global magnetic field, requires specificity in the targeted module's reaction, and thus the module acts differently than the other modules. To date, a few approaches have attained remotely controlled micro-robot addressing. Frutiger et al. (2009) and Diller et al. (2011) employ magnetism to actuate micro-modules independently. Their models exploit the distinctive responses of the modules to frequencies of the externally applied magnetic field, attaining simultaneous control of the micro-modules. Donald et al. (2006) employ an electrostatic field and attain an independent control of four micro-modules. In a unique approach, Pawashe et al. (2009) developed micro-assemblies by selectively anchoring micro-modules with electrostatic surfaces. While modules staying on specific surfaces are clamped, other modules can be remotely directed. This method enables not only the reconfiguration of modules, but also allows the connections between modules to be sustained by magnetic forces. One of the shared characteristics of these approaches is that they mostly exploit the advantages of top-down control; each module is

mainly affected by externally applied magnetic/electrostatic fields, without explicit inter-modular interactions. The restrictions on performance are mainly due to the possible heterogeneity levels of the modules.

A natural system (biological and chemical), on the other hand, takes a contrasting approach to complex assembly, a bottom-up approach. The main driving incidence for assembly is molecular interaction, which results in massive parallel reactions in the abundant molecules (e.g. proteins synthesize into tissues in a distributed way). Researchers have been attracted by such an amazing capability and have attempted to reproduce this behavior in engineering, employing various physical mechanisms for the attachment and detachment of modules. Physics provides various interactive channels for inter-modular interactions across various scales (Whitesides and Grzybowski 2002). This section outlines the relevant and major mechanisms of inter-modular interaction in studies of assembly systems on various scales. A well-summarized overview of self-assembly systems, from milli- to nanoscales, can be found in Mastrangeli et al. (2009) and Bishop et al. (2009).

Magnetism has been a favorite of engineers for a long time, due to the long-range intrinsic property of a zero energy cost force exertion. A few employed magnetism for the driving factor of assembly at the micro scale. Love et al. (2003) showed the 3D self-assembly of metallic rods with submicron diameters. The process is prompted by the module magnetic interactions. Shetye et al. (2008) demonstrated magnetically-directed self-assembly of 1 mm sized components into an ordered array on a planar substrate. 2500 micro-components assembly, showing a high assembly yield by combining magnetic force, shape recognition, and vibration, is presented in Ramadan et al. (2007). The model from Klavins et al. realized detachment by swiveling permanent magnets from the connection sites. Their module is capable of making decisions on maintaining a connection to the neighbor module, referring to the global configuration (Napp et al. 2006; Klavins 2007). Mermoud et al. combined magnetism and fluidic turbulence to represent the assembly and disassembly of floating modules. They developed a formal and generic computational framework for modeling and controlling stochastic distributed systems that can be achieved in real-time (Mermoud et al. 2012).

One of the problems in using magnets is the inflexible property; the magnetic polarities are normally fixed and cannot be regulated. Numerous efforts have been devoted to the development of advanced magnets that can adjust their strength, thus enabling flexible adhesion. One of the earliest examples of controlling magnetism was by Feiner et al. (1960), where a ferrite core, wound with a metallic reed, changed its magnetization when receiving magnetic field pulses from different directions. Their work aims to realize a magnetically controlled mechanical relay. A distinct attempt at a switchable magnet can be seen in the work of Israelton (1969), where a manually-changed direction of one of the two aligned magnets opens or hides the magnetic flux, causing either magnetic attraction or the magnetization to be switched off. Further attempts were carried out by Edgar et al. (Edgar et al. 1972). Their model consists of a permanent magnet wrapped with a coil. The magnetization can be switched off by keeping a current running to the coil. A more advanced model was proposed by Braillon (Braillon 1978). The Series Electropermanent Magnet has serially-coupled magnets, made of a combination of high-coercivity material and low-coercivity material, which can swap magnetic flux paths by passing pulsed currents to the low-coercivity magnets. Different from Braillon (1978), Pignataro (2001) arranged magnets with two different coercivities in parallel and realized an electropermanent magnet. Gilpin et al. (2010) realized an electropermanent magnet used as a connector for modular robots. Connection mechanisms that utilize magnetic turn-

off characteristics have been applied to various climbing robots, such as with Schempf et al. (1995) and Rochat et al. (2010). Diller et al. (2012b) achieved a remotely realizable electropermanent magnetic system. The realized micro-pumps consist of a mixture of high-coersive magnetic material and low-coersive magnetic material, and an externally pulsed magnetic field enables a low-coercivity material to switch the orientation of magnetization, eventually causing the net magnetization to become zero.

Among the numerous attempts to develop functional micro-assembly mechanisms, the most elemental but significant approach exploits the mechanical features. Cohn and Kim (1991) took a hint from crystal annealing, and demonstrated that 1000 mm-size components self-assembled onto a 2D plane. Penrose (1958) may be the first to envisage the importance of connection mechanisms in the context of autonomous systems. His model employs a mechanical hooking mechanism that can be repeatedly released. This is a significant issue when developing mechanical connections. Penrose and Saitou et al. paid close attention to the "releasable" mechanical connection mechanisms by modifying the connections reactive to their inputs (Saitou and Jakiela 1995; Saitou 1999).

The electrostatic force has been utilized, especially for docking miniature objects (Grzybowski et al. 2003). Böhringer et al. (1998) employed electrostatic forces for assembly, assisted by ultrasonic vibration for the agitation. Dejeu et al. (2009), realized the attraction and repulsion of micro-components by altering the environmental chemical pH, which switches the electrostatic state of a component. The method is also applied for clamping or controlling micro-robots (Donald et al. 2006; Floyd et al. 2009a). Despite the size being macroscopic, Karagozler's model (2007) attains not only connection by electrostatic force, but also inter-module power transmission and communication.

Constant fluid flow can be used for the adhesion of two modules. One of the earliest attempts in the field of robotics was by White et al. (2005), which has lately been improved in Tolley et al. (2010). The creation of spatial patterns with multiple miniature components is shown in Grzybowski et al. (2004). The fluid dynamics that keep the component distances are generated by the components themselves being rotated, induced by a rotational magnetic field. The control of the flow is an issue with this method. To keep the connections, the systems normally require a constant flow or an additional connection mechanism.

The capillary force has been a subject of study for the adhesion of miniature objects assembly for a long time, though only recently has this been brought to light. Hosokawa et al. (1996) employed the capillary force for the self-assembly of floating micro-components. Rothemund et al. (2000) conducted exclusive disjunction (XOR) using a lateral capillary force for their floating units. Reversible self-reconfiguration, by changing the environment, can be found in Mao et al. (2002). Observations on different assembly patterns, are changing the edge properties, can be found in Wolfe et al. (2003). Micro-assembly using capillary force can be found in Zhou and Chang (2006), and further realizing a display with a similar method can be found in Jacobs et al. (2002), while the structuring can be found in Randhawa et al. (2010).

Assembly systems combined by chemical state changes have been utilized by several groups. Applications by Gracias et al. (2000) and Boncheva et al. (2003) are known for the use of solder for physical and electrical connections. Through the connections, the implemented circuits can be further extended to the connected modules. Hydrogen bonding using thermal cycles is proposed in Miyashita et al. (2008). The mechanism exploits the characteristics of the media (water, in this case) and changes the physical phase from liquid to solid, depending on the temperature. **?**)

employed Hot-Melt-Adhesive for the climbing wall mechanism. A mercury robot is attempted and demonstrated in Yokoi et al. (2003) as an extreme shape of robot.

1.2 Motivation

As with biomolecular systems, some of the approaches mentioned above exploit an advantage of localized physical interactions. This study scopes the same focus; we seek the advantage of the bottom-up approach. Suppose there is a task that we regulate, adjusting the distance between two modules, as shown in Figure 1 (a) and 1 (b). In the typical top-down approach, the operator (controller) compasses the global position of each module, escorted by some feedback information regarding the system's state, such as visual feedback (Figure 1 (a)). This can be done, in the bottom-up manner, by using the magnetic forces of the two magnets to alter the strength, such that they regulate the distance by themselves (Figure 1 (b)). That is, if the interaction is performed between magnets mounted on modules, one prospective controlling method can regulate the magnetism in a top-down manner and indirectly alter the interaction. The benefits of using this method for assembly are twofold: (1) a low central computational cost (could be attained by the feed-forward manner), and (2) a robust assembly process that protects against physical turbulence. The robustness is mainly derived from the parallel assembly path, which theoretically has no limit, and the large amount of playing modules, which could be replaced continually by other modules. Figure 1 shows the potential for enriching the system's addressability by coupling these approaches in a further manner. However, the challenges in a bottom-up approach are (1) how to control the behavior as you task, such as when to start and stop the action, and (2) how to keep generality in application, such as maintaining versatile applicability rather than having molecules designed for specific tasks.

[Insert Figure 1]

In this paper, in consideration of these concerns, we design and build a method for the robust assembly and reconfiguration of micro-modules, using inter-module magnetic interactions as the main driving scheme. We first focus on the remotely tunable magnets proposed by our group (Diller et al. 2012b) for the solution of addressability. We then design a control scheme, which enables both an easy system design and applicability to complex models, in Section 2. Based on the designed scheme, we develop our system and introduce in Section 3. We examine the validity of the model by conducting simple attachment and detachment between two modules' tasks in Section 4.1. In Section 4.2, we carefully analyze the system's properties and demonstrate magnetic micro-module reconfiguration with three modules. In Section 5, we further discuss the applicability of the model to increased numbers of modules, and we offer a conclusion in Section 6.

2 Methods

This section presents the basic methods of our approach, starting with how to achieve module addressability using heterogeneity in a multi-magnet system, followed by the conditions for interaction, and concluding with how the method is used in a reconfigurable system.

2.1 Introducing Heterogeneity by Coercivities

This work is grounded in micro-robotics research that employs a magnetic field for actuations (the externally applied magnetic field for actuations is hereafter termed $H^{\pm}_{act}$, where $\pm$ denotes the direction of the field). Generally, in order to remotely manipulate multiple magnetic modules with a single magnetic field, the designer has to provide addresses either to the space (Floyd et al. 2009a) or to the modules. Given that we treat N ($\in \mathbb{N}$) number of modules, the way of addressing modules can be introduced in various manners: by differentiating the shapes (or the mass) of soft magnetic bodies (Diller et al. 2011), by the capacitance level (Donald et al. 2008), or by using body-mass distributions accompanied by different magnetizations, so that modules respond to different resonance frequencies (Frutiger et al. 2009).

In this study, we achieve heterogeneity in magnetization by providing a corresponding number of magnetic materials that feature different coercivities, and we thus exhibit distinctive responses to applied magnetic fields. Namely, we exploit the differences in coercivities among magnetic materials: one switches its magnetization without hysteresis by H_{act} (i.e. a soft magnet, coercivity $H_{c,soft}$), another switches with hysteresis, using a strong pulsing magnetic field (hereafter termed $H^{\pm}_{pulse}$) (a hard magnet, coercivity $H^{\pm}_{c,hard1}$), and the last keeps its magnetization, regardless of the applied fields (a hard magnet, coercivity $H^{\pm}_{c,hard2}$). We illustrate the image in Figure 2 (a), with a magnification of the corresponding division on the right. When we have $H^{+}_{c,soft} < H^{+}_{c,hard1} < H^{+}_{c,hard2}$, by applying a magnetic field H^{+}_{act}, whose strength is between $H_{c,soft}$ and $H_{c,hard1}$ ($H^{+}_{c,soft} < H^{+}_{act} < H^{+}_{c,hard1}$), the magnetization of the soft magnet $\boldsymbol{m_{soft}}$ can be switched, while we maintain the rest of the moments. The polarity of magnetic moment $\boldsymbol{m_{hard1}}$ can be switched by applying a relatively strong magnetic field pulse H^{+}_{pulse1} in the desired direction, where the strength of H_{pulse1} should be such that it is $H^{+}_{c,hard1} < H^{+}_{pulse1} < H^{+}_{c,hard2}$. The process can be switched back by applying H^{-}_{pulse1} to the material. Theoretically, the method holds as long as there are materials with distinctive coercivities and field pulses that can be applied with respective strengths[1]. In this way, the magnetic moments can be remotely switched without mechanical access. Note that when applying H^{+}_{pulse2}, $\boldsymbol{m_{soft}}$ and $\boldsymbol{m_{hard}}$ are affected and are caused orientations of magnetizations. However, a prompt application of H^{-}_{pulse1} or H^{-}_{act} can switch the magnetization of the $H_{c,hard1}$ magnet and the $H_{c,soft}$ back in the opposite direction. By iterating this process, decreasing the strength of the field application, the system is potentially capable of altering the specific strength of a magnet. Figure 2 (b) illustrates m-H curves with a smaller sweep of H, where both hard magnets were pre-magnetized to show similar values of m. The important thing to notice is that both m_{hard1} and m_{hard2} keep their signs, either positive or negative, with respect to H, while m_{soft} changes value, from negative to positive. The applied magnetic field H_{act} is controlled by the system, and the maximum values of magnetic moments $\boldsymbol{m_{soft,max}}$, $\boldsymbol{m_{hard1,max}}$, and $\boldsymbol{m_{hard2,max}}$ can be tuned by the volumes (m = volume $\cdot$ magnetization).

[Insert Figure 2]

[1]The fact that using a soft magnet requires the constant application of a magnetic field to maintain magnetization can potentially be a disadvantage. However, this characteristic can be exploited as an advantage, since the magnetization can easily be "switched off" by simply turning off H_{act}. In our work in (Diller et al. 2012b), we employed ferrite as an alterable magnetic material, whose coercivity is $320\,kA/m$. Parts of the work in this paper were presented in (Diller et al. 2012a).

2.2 Lateral Magnetic Interaction and Assembly Control

Magnetic attractive/repulsive forces are used as interactions in our modular system. To understand these interactions, we now present the governing physics. A magnetic moment casts a three-dimensional orbital magnetic flux, which is starting from and coming back to the initial moment. Consider the magnetic modules $\mathcal{M}_i$ and $\mathcal{M}_j$, which feature respective magnetic dipole moments, $\boldsymbol{m}_i$ and $\boldsymbol{m}_j$ $(i, j \in \mathbb{N}, i \neq j)$, separated by a distance $r_{ji} \gg d$ (d : diameter of the magnets). The magnetic flux density at the position of $\boldsymbol{m}_i$, created by $\boldsymbol{m}_j$, can be described with a position vector $\boldsymbol{r}_{ji}$ as:

$$\boldsymbol{B}_{ij} = \frac{\mu_0}{4\pi}\left[\frac{3(\boldsymbol{m}_j \cdot \boldsymbol{r}_{ji})\boldsymbol{r}_{ji}}{r_{ji}^5} - \frac{\boldsymbol{m}_j}{r_{ji}^3}\right], \tag{1}$$

where $\mu_0 = 4\pi \times 10^{-7}\,\mathrm{H/m}$ is the permeability of free space.

The magnetic force and the torque acting on $\boldsymbol{m}_i$, due to $\boldsymbol{m}_j$, are respectively given as:

$$\boldsymbol{F}_{ij} = (\boldsymbol{m}_i \cdot \nabla)\,\boldsymbol{B}_{ij} \tag{2}$$

$$\boldsymbol{\tau}_{ij} = \boldsymbol{m}_i \times \boldsymbol{B}_{ij}. \tag{3}$$

Suppose there is a third magnetic module, $\mathcal{M}_k$, featuring magnetic moment $\boldsymbol{m}_k$ $(k \in \mathbb{N}, k \neq i, j)$. It becomes *three body problem* when estimating the interaction of three magnets in a space, and therefore designing the arbitrary motion path is recognized as a non-trivial task. In order to reduce the postural complexity of multiple magnetic moments, we constrain the orientation of the magnets and restrict the work area to a 2D plane (Figure 3 (a)). In this way, magnets are aligned perpendicularly to the plane, and they only laterally interact with each other, which results in a simplification of the description level of the system. Due to the fixed posture, there are three degrees of freedom for each magnetic module (x, y, and *yawing*)), and for a system with N modules it is $3N$. In this study, we apply magnetic fields H_{act} and H_{pulse} perpendicularly to the modules' motion plane, as illustrated in Figure 3 (a). We define the magnetic field direction positive (+) that goes along the increasing z-axis, and define negative (−) *vice versa*.

[Insert Figure 3]

When the magnets are parallel and coplanar, as in Figure 3 (a), the torque becomes zero, and the force simplifies to:

$$\boldsymbol{F}_{ij} = \sigma_{ij}\,\frac{3\mu_0}{4\pi}\frac{m_i m_j}{r_{ij}^5}\boldsymbol{r}_{ji}, \qquad \sigma_{ij} = \frac{\boldsymbol{m_i} \cdot \boldsymbol{m_j}}{|\boldsymbol{m}_i||\boldsymbol{m}_j|}, \tag{4}$$

implying that the attraction and repulsion of two magnets is determined by the orientation, and the magnetic force simply decays in inverse proportion to the distance to the power of four ($F \propto r^{-4}$). The torque acting on a single module is zero. This is the great advantage of the system, as when designing the interactions of the modules, we only need to take the distances into account[2].

[2]The reliability of the derivation of force value when $r_{ji} \approx d$, assuming dipoles have volumes, was checked and verified with COMSOL finite element analysis.

Considering that magnetic energy U_{ij} is given by

$$U_{ij} = -\boldsymbol{m}_i \cdot \boldsymbol{B}_{ij}, \tag{5}$$

it can be simplified to:

$$U_{ij} \quad = \quad \sigma_{ij} \, \frac{\mu_0}{4\pi} \frac{m_i m_j}{r_{ij}^3}, \qquad \sigma_{ij} = \frac{\boldsymbol{m_i} \cdot \boldsymbol{m_j}}{|\boldsymbol{m}_i||\boldsymbol{m}_j|}. \tag{6}$$

We can determine the total magnetic potential energy of the system as

$$U_{mag} = \sum_{i>j} U_{ij}. \tag{7}$$

Suppose the positions of m_i and m_j are fixed, and m_k is free to move on the plane. The U_{mag} at each spatial position of $m_k(x, y)$ can be derived from Eq. (7) as a scalar value, as shown in Figure 3 (b). When m_k is placed at the position seen in Figure 3 (b), the moment follows the path colored red. The system acts to minimize U_{mag} over time. When m_k is flipped in the opposite direction, the look of the U_{mag} is turned upside down, causing an attraction between m_i and m_k, while causing a repulsion between m_j and m_k. As a result, m_k is delivered in the opposite direction, as in Figure 3 (b). From the system's point of view, the switching action, when the switched module is next to another module, causes a sharp rise in U_{mag}, instantly unbalancing the system, allowing the energy to be consumed for a conversion to a stable state, which is accompanied by a physical reconfiguration.

Figure 4 shows a state transition diagram representing the possible configurations with three different magnetic modules. This is the methodology we plan to use further in our practice. Here we assume the three modules include (1) a module with a soft magnet (e.g. Fe, the module is symbolized as $\mathcal{F}$), (2) a module with a high coercivity magnet (e.g. Neodymium Iron Boron: NdFeB, symbolized as $\mathcal{N}$), and (3) a module with a medium coercivity magnet (e.g. alnico, symbolized as $\mathcal{A}$). The possible configurations with $\mathcal{F}$, $\mathcal{N}$, and $\mathcal{A}$ are: $\mathcal{F}(\uparrow) - \mathcal{N}(\downarrow) - \mathcal{A}(\uparrow)$, $\mathcal{N}(\uparrow) - \mathcal{F}(\downarrow) - \mathcal{A}(\uparrow)$, $\mathcal{F}(\uparrow) - \mathcal{A}(\downarrow) - \mathcal{N}(\uparrow)$, and $\mathcal{F}(\uparrow) \;\; \mathcal{N}(\uparrow) \;\; \mathcal{A}(\uparrow)$, where "$-$" denotes a physical contact, arrows denote the orientation of the magnetic poles, and we count mirror symmetric patterns as one, assuming they have the same configuration topology. In this study, we remotely control the magnetization of $\mathcal{F}$ and $\mathcal{A}$ by externally applying magnetic fields, while $\mathcal{N}$ stays the same. As we describe in Section 2.1, we employ two distinctive magnetic fields: one, with a low strength, that can only affect soft magnets ($\mathcal{F}$), but is applied for a duration (H_{act}), and another, with a high strength, that can alter medium coercivity magnets ($\mathcal{A}$), but is impulsive (H_{pulse}). Transitions for these four states can be deterministically made by applying $H_{act}^{\pm}$ or $H_{pulse}^{\pm}$. Stronger H_{act} causes $\mathcal{F}$ to be placed farther from $\mathcal{N}$ and $\mathcal{A}$, and this can be counted as the fifth state (see path 9 in Figure 4).

[Insert Figure 4]

3 System Design

The system's design consists of four sections: the selection of magnetic materials and their tuning (Section 3.1), the module fabrication (Section 3.2), the liquid-liquid surface design (Section 3.3), and the LC circuit design and the employed apparatus for applying aimed magnetic fields (Section 3.4).

3.1 Selection of Magnetic Materials and their Tuning

Having considered the necessary requirements, we selected Fe for the soft magnetic material, partly due to the high slope of the m-H curve around $H_{act} = 0$. For the medium coercivity magnet, anisotropic alnico was chosen, due to the relatively low slope. As for the hard magnet with high coercivity, NdFeB was chosen for its relatively constant magnetization, regardless of an external magnetic field within a range of H_{act}. Figures 5 (a) and 5 (b) show experimental plots of the magnetic moments of the NdFeB, Fe, and alnico pieces that we will implement in the modules in Section 3.2 (m_{NdFeB}, m_{Fe}, and m_{alnico}) versus the applied field (H) obtained by alternating gradient force magnetometer (AGFM, Princeton Measurements MicroMag 2900). Figure 5 (a) shows the m-H loop of three magnetic materials, under the application of magnetic fields, up to the machine's maximum performance (1.114×10^6 A/m). Here, the volume of each magnetic material was tuned before the measurement, such that the absolute maximum values were nearly equal to the previous measurements. The differences in the coercivities are clearly seen, and compared to the large hysteresis of NdFeB and alnico, a linear behavior can be observed in Fe.

[Insert Figure 5]

Figure 5 (b) illustrates m-H curves with a smaller sweep of H (11.9×10^3 A/m) corresponding to the Fe switching field. The magnets were respectively pre-magnetized, as we expect to use in the developed system (NdFeB under 660×10^3 A/m and alnico under 63.1×10^3 A/m). It can be seen that NdFeB is merely influenced by H, while Fe linearly changes the value from negative to positive, and the two alnico samples keep their signs either positive or negative, with respect to H (cf. Figure 2 (b)). Note that these samples are what we implemented in the modules and used in the experiments.

3.2 Module Fabrication

The magnetic force between magnets increases in a nearly inverse proportion to the distance to the power of four (Eq. (4)). Reducing the distance of two magnets so that they are very close creates strong forces and torques, causing instability in the system. To avoid this problem, the magnet (termed the "core") is surrounded with a polyurethane "shell", as shown in Figure 6 (a). Also, a shell should prevent the magnetic cores from magnetically interfering with each other and affecting the original magnetization levels.

[Insert Figure 6]

The geometries of the cores will vary due to the different demagnetization factors. The areas along the x-y-plane are similarly set, while lengths along the z-axis are adjusted, such that they exert appropriate magnetizations. The shapes of the shells were designed to be flat, so that they float stably on a liquid surface, resistant to rolling and pitching motions. To investigate the distributions of the magnetic field created by each magnet, we applied a finite element method, using commercially available software (COMSOL), and plotted the results in Figure 6 (b). The size and the shape were determined also by taking into account several experimental and fabrication conditions. First, in order to minimize the inertial effect of the modules, the size was set to be smaller than several millimeters (for a low Reynolds number environment). Second, considering the minimum size of the magnet to avoid destroying the magnetic domains, the size of the core was set to a few dozens of micrometers. Eventually, being constrained by the strength and the form of the magnetic field, which was affected by the size of magnet, the size and the shape of shell were determined. We specifically considered the influence on the alnico core, in that the coercivity (the magnetic field strength that can be affected by an external magnetic field) is 41.59×10^3 A/m. The shell size was set to 750 μm in diameter, such that the body fully covers the contour of the norm of one tenth of the coercivity (41.59×10^2 A/m). Practically, our fabrication technique allows the module to be sized down to dozens of micrometers. We summarize the specifications of modules in Table 1. The fabrication process for a module is shown in Appendix B.

[Insert Table 1]

3.3 Liquids Interface Design

The prerequisites for the experimental environment are as follows: (1) to enable a smooth lateral motion for the modules, with little friction; (2) to restrict the modules' motion on a two-dimensional plane; (3) to provide a gravitational force toward the center of the environment, forcing interactions in density, and avoiding modules from gathering on the boundary; (4) to minimize the surface energy of all involved components; and (5) to provide a damping action with viscosity.

To minimize friction, the modules were settled on a water surface. To satisfy prerequisites (3)-(5), we added a polydimethylsiloxane (PDMS) layer (Clearco Products) on top of the water layer, and surrounded it with a cylindrical glass boundary, as shown in Figure 7 (a). This way, the water surface on which the modules are placed creates a curvature that sags in the middle due to the surface tension with the glass boundary, which causes modules to gather around the center due to the gravity, allowing them to maintain sufficient magnetic and physical interactions. The surface energy density of PDMS is 0.030 J/m^2 at 20° (cf. water is 0.072 J/m^2), the viscosity is 5 cSt[3], and the density is $\rho = 918\,\mathrm{kg/m^3}$. Therefore, it reduces adherence among the modules, stabilizes the modules' motion while maintaining high damping action, and enhances the flotation of modules, with a buoyant force arising from the high density, in comparison to the air, and its hydrophobic properties, which attract modules made of hydrophobic material. This also helps to reduce the capillary influence (described below) among the modules.

[3]The viscosity can be differentiated according to tasks.

The height h of the water surface can be derived using the linearized Laplace equation (Bowden et al. 1999):

$$\frac{\partial^2 h}{\partial x^2} = \frac{1}{\gamma}(\Delta\rho g h - \Delta P_0), \tag{8}$$

where γ is the interfacial energy density between the water and the PDMS ($0.042\,\mathrm{J/m^2}$), $\Delta\rho$ is the difference in the densities of the two liquids ($82.0\,\mathrm{kg/m^3}$), and g is the gravity ($9.8\,\mathrm{m/s^2}$). We set the origin of the global coordinate at the center of the container in the x-y-plane and at the lowest position of the surface. ΔP_0 is the change in pressure across the interface at $x = 0$ (Pascal).

By applying conditions where $\Delta P_0 = 0$, since there is no fluid flow on a surface, $h(0) = 0$ is the origin of the coordination, and $1.11 \cdot 10^{-3}\,\mathrm{m}$ is the experimentally measured maximum height difference between the center and the boundary (see Figure 7 (b)), and by extending the model to a two-dimensional space model, premising that $h(x, y)$ shows an equal height all around at an ideal boundary, we find the solution as:

$$h(x, y) = 16.39 \cdot 10^{-4}\{\cosh(19\sqrt{53(x^2 + y^2)}) - 1\}. \tag{9}$$

We numerically derive the surface curve as displayed in Figure 7 (a) and 7 (b) (an angled view in 7 (a), and a side view, with a comparison with the real surface curve, in 7 (b)). Some errors can be recognized at the border, which we assume is due to the hydrophobicity influence of the glass container. Also, in practice, variances usually exist in the height of the water surface at the container border. Figure 7 (c) shows the layers in which the module bodies are present. Modules are placed vertically with their sides facing up, and situated between two liquid layers. The two layers are formed in a tilted plastic container where the water layer creates negative menisci, providing modules with a vertical surface on which to stand horizontally (see Figure 19 in Appendix C for the composition). In this way, we can observe the module bodies' placement in layers, as well as the surface terrain, which only reflects the capillary influence between modules without the hindrance of surface deformation due to the modules' weight. The photo shows that most of the module bodies are in the PDMS layer (note that the body parts in the water layer are reflections). We measured the volumes of the Fe, alnico, and NdFeB modules as $88.6 \cdot 10^{-12}\,\mathrm{m^3}$ $78.9 \cdot 10^{-12}\,\mathrm{m^3}$, and $79.8 \cdot 10^{-12}\,\mathrm{m^3}$, respectively. We estimated the module's masses, as shown in Table 1, considering the properties of the constituent materials. By taking into account the density of PDMS, we estimate the masses counting buoyancy of these modules as $14.5 \cdot 10^{-8}\,\mathrm{kg}$, $4.71 \cdot 10^{-8}\,\mathrm{kg}$, and $5.62 \cdot 10^{-8}\,\mathrm{kg}$. From these values, the floating of the modules is assisted by the surface tension of the water, as illustrated in the small window in Figure 7 (c). A glass container was fabricated from the glass tube, as shown in Figure 7 (b).

[Insert Figure 7]

The selection of PDMS and water as supportive liquids for modules enables a global interfacial surface design that was desired for the experimental tasks, although on the other hand, it also introduces capillary interaction between modules (capillary length is estimated as $7.20 \cdot 10^{-3}\,\mathrm{mm}$).

We minimized the influence of capillary force by selecting polyurethane as the material of the modules' shell, such that modules reside in the PDMS layer due to rather hydrophobic characteristics, and hence barely create a meniscus (see Figure 7 (c)). Nevertheless, we estimate the magnitude of capillary force that could potentially act between two proximate modules premising several contact angles of water surface. The capillary energy, U_{cap}, created by a single module can be calculated as (Hosokawa et al. 1996):

$$U_{cap} = \int_y \int_x \frac{\gamma}{2} \Big[\left(\frac{\partial h}{\partial x} \right)^2 + \left(\frac{\partial h}{\partial y} \right)^2 \Big] dxdy. \tag{10}$$

Here, $h(x, y) = 1.9 \cdot 10^{-3} \cdot \cot\theta \cdot \exp(\frac{-\sqrt{x^2+y^2}}{1.9 \cdot 10^{-3}})$ is the height of the water surface derived from Eq. (8), in which the origin of the coordinate is set at the edge of the module, and θ is the contact angle of the surface measured down from the vertical axis (see Figure 20 in Appendix C for a horizontal view of a floating module). By integrating over the container area (8 mm across), we obtained $U_{cap} \approx 4.35 \cdot 10^{-12}$ J when the contact angle is 88°, $U_{cap} = 2.73 \cdot 10^{-11}$ J at 85°, and $U_{cap} = 1.11 \cdot 10^{-10}$ J at 80°. The results suggest that when the surface contact angle is about 85° or less, the capillary energy and the magnetic energy have the same order of magnitude, and thus influence to the system (ref. Section 4.2).

The gravitational potential energy of liquids created by a module caving in the water layer, U_{liq}, can be approximated and derived as (Hosokawa et al. 1996):

$$U_{liq} = \int_y \int_x \frac{\gamma}{2} (kh)^2 dxdy, \tag{11}$$

where $k = \sqrt{\frac{\Delta\rho g}{\gamma}}$. Consequently, we obtained $U_{liq} = 1.59 \cdot 10^{-17}$ J at contact angle = 88°, $U_{liq} = 9.95 \cdot 10^{-17}$ J at contact angle = 85°, and $U_{liq} = 4.04 \cdot 10^{-16}$ J at contact angle = 80°. The values show that the influence of the gravitational potential energy of liquid deformation by a module is much less than the magnetic potential energy ($\approx 10^{-11}$ J, ref. Section 4.2). We think that the main reason for this must be the comparable densities of two liquid layers, as well as the light weight of the module.

3.4 LC Circuit and Coil Layout

In order to realize the effective magnetic fields of H_{act} and H_{pulse}, which should respectively reach the strength of $5.0 \cdot 10^3$ A/m and $41.59 \cdot 10^3$ A/m (c.f. Figure 5), the container is interjected with two different types of coils: a pair of pulsing coils and a pair of actuation coils, as shown in Figure 8. For H_{act}, we employ the platform developed by our group (Floyd et al. 2009b). A series LC circuit ($L = 4.82 \cdot 10^{-6}$ H, $C = 32.4 \cdot 10^3$ F, 60 V charged) is employed to generate the high impulsive current flow for H_{pulse} (Diller et al. 2012b). Note that the applicable H strength is restricted by specs of the experimental coil system, such as the applicable current amount and the profiles of the coils. A camera is placed on the top of the setup.

[Insert Figure 8]

4 Experimental Results

In the experiments, we investigated the system's performance in magnetization switching by carrying out attraction/repulsion tests on two modules (Section 4.1) and then operating reconfiguration tasks with three modules (Section 4.2).

4.1 Attraction and Repulsion With Two Modules

This section demonstrates a reversible magnetic connection (attachment and detachment) in the simplest way: placing two modules on the designed surface and showing attraction/repulsion by switching the magnetization of one of the modules (see Figure 9 (a)). The distance between the two repelling modules equipped with the magnetic moments $\boldsymbol{m}_i$ and $\boldsymbol{m}_j$ can be estimated by examining the terrain of the system's potential energy (U_{total}), which is a sum of the magnetic potential energy (U_{mag}) and the gravitational potential energy (U_{grav}).

$$\begin{aligned} U_{total} &= U_{mag} + U_{grav} \\ &= \sum_{i>j} \sigma_{ij} \, \frac{\mu_0}{4\pi} \frac{m_i m_j}{r_{ij}^3} \\ &\quad + \sum_i M_i \cdot g \cdot 16.39 \cdot 10^{-4} \{\cosh(19\sqrt{53(x_i^2 + y_i^2)}) - 1\}, \;\; \sigma_{ij} = \frac{\boldsymbol{m_i} \cdot \boldsymbol{m_j}}{|\boldsymbol{m}_i||\boldsymbol{m}_j|}, \end{aligned} \tag{12}$$

where M_i is the mass of the i-th module.

In this work, we ignore the effects of module inertia. The magnitude of kinetic energy of a module (U_{kin}), when it is moving at the maximum possible speed, can be estimated as $U_{kin} = \frac{1}{2}Mv^2$, where $M = 2.34 \cdot 10^{-7}$ kg (the mass of the heaviest module $\mathcal{F}$) and $v = 1.37 \cdot 10^{-3}$ m/s (one of the fastest translational motion speeds observed in the experiment in this section). We obtain $U_{kin} = 2.22 \cdot 10^{-13}$ J, which is two orders of magnitude smaller than the magnetic potential energy U_{mag} ($\approx 10^{-11}$ J, see Section 4.2), suggesting a small influence of kinetic energy of the module on motion compared to magnetic energy.

Figure 9 (b) and 9 (c) visualize numerically derived U_{total} of the case with the $\mathcal{N}$ and $\mathcal{F}$ pair, placing a relatively heavy module ($\mathcal{F}$) at the center of the container ($[0, 0]$ in the coordination) as the representative example. 9 (b) is when applied H_{act} is 500 A/m, while 9 (c) is when applied $H_{act} =$ 8000 A/m. The resting position of the second module is where the U_{total} becomes the minimum in the plot. Therefore, the distances between the two modules are approximately estimated by measuring the length between the center and the global minimum[4]. It can be seen that, as m_{Fe} becomes stronger in respect to the increase in H_{act}, an increase in the resting position (which is the highlighted dot circles) is recognized. This radius is plotted in Figure 9 (d) and 9 (e) (for the $\mathcal{N}, \mathcal{F}$ pair in 9 (c) and for the $\mathcal{A}, \mathcal{F}$ pair in 9 (d)), together with the experimentally observed distances of the two modules under respective H_{act} strengths. The experimentally obtained data are the averages of five samples, with error bars representing standard deviations. In the figures, gradual rising slopes, along with an increase of H_{act} strengths, can be seen in both the theoretical curves

[4]To be precise, this is not accurate for the three-dimensional movement of modules. Ideally, U_{mag} and U_{grav} should be independently measured to derive the global minimum of U_{total}. However, since the effect of U_{grav} around the center is small, we premise that the heavier module stays at the center of the coordinate.

and the experimental curves. Both lines show symptoms of saturation, though this should occur at much higher field strengths, judging from the results in Figure 5.

[Insert Figure 9]

Figure 9 (f) shows a similar plot, where we vary the applied H_{pulse} strength for the $\mathcal{N}, \mathcal{A}$ pair and display both the theoretical and experimental plots. The slope of the theoretical plot in 9 (f) shows linear growth. This is supposedly because the increase in strength of m_{alnico} is nonlinear to the increase of H_{pulse}, showing further room to strongly repel the $\mathcal{N}$ by accepting stronger H_{pulse}. The major reason for the gaps between theoretical estimation and the experimental results recognized in Figure 9 (d)-(f) is presumably because of the imprecise physical installations of the surface terrain, as well as the magnetic materials; when modules were distant, the error in overestimating the liquid surface curvature was influential. Due to the small size and relatively shallow depth of the container, we suspect there might have been more flat places on the surface in the experiment, which allowed modules to stay farther apart.

The magnitudes of other factors, especially the capillary force between two modules and gravitational influence by liquids' deformation due to modules' weight, can potentially be intensified in correspondence with the change of contact angles. The discrepancies between theoretical curves and experimental plots in Figure 9 (e) and 9 (f) when small H_{pulse} or H_{act} is applied show similar trends. If the common module in both experiments floats in a manner that causes a rise in the contact surface, this might be a reason for the variance. In this case, the defect can be amended by selecting a truly hydrophobic material for the shell. Other forces, such as surface adhesion and electrostatic attraction, may cause delays in rising timings of the experimental slopes. These forces depend on the surface energy and dielectric properties of the materials used for the modules and the operational medium, and thus it is difficult to eliminate them without interfering with other factors.

4.2 Reconfiguration Task With Three Modules

To study the attributes of a system when there are three modules, we derive and plot the total potential energies of the system U_{total} on the x-y-planes, under the premise that the contact points of the two modules are positioned at the center of the container $[0, 0]$. The case when $\mathcal{N}$ and $\mathcal{F}$ are in a pair, and $\mathcal{A}$ is assumed to be in transition, is in Figure 10 (a)-(b), and the case when $\mathcal{N}$ and $\mathcal{A}$ are in a pair, and $\mathcal{F}$ is in transition, is in Figure 10 (c)-(d). We display the contours of module shells with red circles, giving a certain height for visualization. Knowing that the center of a third module cannot reach inside the blue circles, meaning the "third module's reachable position", we keep depicting the terrain of U_{total} up to half of the module radius. This is to show the sharp increase/decrease of U_{mag} near the magnetic cores, as well as for a future experiment with smaller modules. The estimated trajectories of translating modules are mapped as stream lines onto each energy surface.

[Insert Figure 10]

Overall, the model does well predicting the behavior of switched modules. Both figures show there is no noteworthy "dead region" where a translating module could be trapped and the system could not attain reconfiguration. Also, judging from the figures, the estimated paths of the translating module seemingly do not move far from the repulsive modules and they reach to the back of the attractive module. Our theoretical estimation does not count physical collisions between modules, allowing module bodies to be crossovered. Considering the un-ignorable adhesion force between modules, the paths should ideally be designed to pass farther from the repulsive module, returning to the real back end of the attractive module. In general, the repulsive force exerted by $\mathcal{N}$ decays fast, and hence the translating module ($\mathcal{A}/\mathcal{F}$) experiences little translational force. This suggests that using a wider container, or utilizing liquid-pairs that show more flat central surface, will make the reconfiguration process ideal. The effect should be reflected in the translating module having a longer traversing distance. Besides this, due to the heavy weight of $\mathcal{F}$, the outer terrain in Figure 10 (c) shows a relatively steep curve toward the boundaries, as compared to 10 (a). This influence, caused by the difference in U_{grav}, can be seen in the wider arc of the module's path in 10 (a), in comparison to 10 (c).

In Figures 10 (b) and 10 (c), we plot the experimentally observed trajectories of a translating module, with the respective starting positions and ending positions (with a local coordination seen from $\mathcal{N}$), overlaid by the streamlines of the expected magnet's trajectory for reference. In the experiment, we first placed three modules ($\mathcal{F}$, $\mathcal{A}$, and $\mathcal{N}$) in contact, aligned with the magnetizations ($\downarrow$), ($\uparrow$), and ($\downarrow$), respectively. We then switched the magnetization of the module placed at the end, leading the module to eventually be connected to the opposite module (see also Section 2.2). This reconfiguration process was iterated until ten successful trials were achieved. As predicted from the mathematical model, the observed paths of the third module were close to those from the first and second modules. Apart from the differences in traveling distances, the look of the successful trajectories is similar, showing the reliability of the experiment, which was predicted in the theoretical model. During the experiments, three assembly failures were observed in both cases (76.9 % success rate, marked as "$\times$" in the figure). The shared characteristic of the failed trials was module pairs that had been pulled toward the boundary of a container, hindering the free movement of a translating module. We suspect that this is due to the non-uniformity of the magnetic field H_{act} along the horizontal axes (x-y) created by the coil system. In this case, adjusting the center of the container more precisely to the center of the coil should improve performance. An unintended motion, illustrated with the label $*$ in Figure 10 (a), is likely due to the influence of the asymmetric geometry of $\mathcal{F}$, which may have caused a disturbed flux distribution.

We demonstrated all the transition paths, which appear in Figure 4 (path 1 to path 10), and show the snapshots as a time series in Figure 11 (a)-(u) (see Extension 1). Since all the transitions are reversible, the initial configuration can be set to any configuration. It was set to $\mathcal{N}(\uparrow)-\mathcal{F}(\downarrow)-\mathcal{A}(\uparrow)$ (Figure 11 (a)). By applying $H^{\pm}_{act}$ and $H^{\pm}_{pulse}$, we demonstrated the transformations in Figure 4, following the paths in the order of $1 \to 3 \to 5 \to 7 \to 1 \to 2 \to 8 \to 6 \to 4 \to 9 \to 10$.

[Insert Figure 11]

We track the positions of the modules and derive the magnetic potential energy (U_{mag}, Eq.(7)), which is shown in Figure 11 (v) as a time evolution. The corresponding time domains displayed in

the snapshots are indicated with dotted lines (Figure 11 (a)-(u)). Principally, impulsive rises in the energy levels are observed when H_{act} or H_{pulse} is applied. The energy states are increased, such that the system can use them for reconfiguration. The conversions last until the system reaches a stable formation. Among the pulses, two distinctive types of pulsing potential are recognized: one with high peaks, such as 11 (a), 11 (j), and 11 (r), and the other with low peaks, such as 11 (f), 11 (h), 11 (m), and 11 (p). Pulses featuring high peaks are observed when the polarity of a module positioned in the middle of three modules is switched. Similarly, pulses with low peaks are observed when the switched module is positioned at the side of three modules. In this case, when all the magnetizations are exactly the same, the peak value should theoretically stay below zero; this implies that the attractive forces are more "dominant" than the repulsive forces during the entire transition process. When three modules are all repelling (e.g. Figure 11 (c)), the value is always shown above zero. An application of H_{act} or H_{pulse} introduces attraction to the modules, dropping the energy state below zero. Knowing the magnetization levels of all the modules, the curve tells us not only the event that occurred, but also detailed information on module configurations. As the intervals between pulses show, the system has room to be improved in terms of more frequent applications of H_{pulse}.

In the system, at the micro scale, the fluidic motion around a module is known to obey Stokes' law, whose drag force, F_{drag}, can be described as $F_{drag} = 6\pi\nu Rv$, where ν is viscosity of the fluid (5 cSt), R is the radius of the module (assuming the shape is a sphere here), and v is the velocity of the module. Using one of the fastest speeds ($1.37 \cdot 10^{-3}$ m/s) observed in Section 4.1, we obtain $||F_{drag}|| \leq 4.84 \cdot 10^{-5}$ N. As a calculation of an extreme case, if a module transits the distance of the body length, $750 \cdot 10^{-6}$ m, at this speed, the energy dissipated into the environment is $U_{drag} = 3.63 \cdot 10^{-8}$ J. The order of magnitude of kinetic energy in our system is thus two orders of magnitude smaller than the magnetic energy. Additionally, the inertial influence can be neglected and we can consider the motion as rather static. Therefore, the model of motion of a module can be $F_{mag} \approx F_{drag}$, and this is time invariant. Since magnetic energy does not decay over time and is only dependent on the spatial positioning, the fluidic influence should only be reflected in the transition speed, but not upon the motion trajectory. Besides the static analysis above, estimation of the average transition time can provide the required time for complex assembly. The experimental result shown in Figure 11 (v) implies that each transition after an application of magnetic field takes less than 5 s, and the time to charge the pulsing system is less than 40 s. Thus the total transition time is approximately 1 minute. Solving the equation of motion involving magnetic force and fluid drag calls for numerical analysis, and this is beyond the scope of this study; thus, this aspect should be investigated further in future work.

Although the primary aim of this work is to investigate the capability of micro self-reconfiguration in a feed forward manner, the system offers the potential to incorporate a feedback mechanism, such as visual feedback. As shown, our system encounters a "yield problem" when the number of modules is greater than four (Figure 13 (j)). Implementing visual feedback may provide the possibility of correcting undesired configurations, such that, when the system encounters the yield problem, the operator can reattempt the execution of a magnetic field with a different strength.

5 Discussions

5.1 Reconfiguration With Four Modules

The aim and scope of this study was to realize micro-assembly with multiple components. To begin with, we examined an advanced model in which four modules co-existed. Figure 12 shows the three distinctive reconfiguration scenarios attained with four modules. We differentiated the cases by which type of module ($\mathcal{F}$, $\mathcal{A}$, or $\mathcal{N}$) exist as single, as well as whether the $\mathcal{N}$s are oriented in the same or the opposite direction, thus attracting or repelling. We focus only on the topology, and therefore count mirror symmetry configurations as one. Looping configurations, which have the identical magnet orientation as other configurations but more connections, are excluded because we consider only one reconnection in one transition. The displayed transformation paths are all confirmed to be reversible under ideal conditions, where modules pointing in opposite directions can always be connected. This means, regardless of the initial configuration, that the system can reach any other configuration during the reconfiguration process. Reconfiguration processes in which there are two $\mathcal{F}$s and two $\mathcal{N}$s are shown in Figure 12 (a)-(e) and in 12 (f)-(i) and 12 (j)-(n), respectively. The instances shown in Figure 12 (f)-(i) represent cases in which two $\mathcal{N}$s are pointing in opposite directions, and thus attracting, whereas those shown in Figure 12 (j)-(n) represent the modules pointing in the same direction, and therefore always repelling. Green arrows denote the transitions that occur when switching the magnetization of $\mathcal{F}$(s), and red arrows denote the switching conditions of $\mathcal{A}$(s).

[Insert Figure 12]

There are three topologies that can be represented with four modules: branch, separated, and linear (we exclude looping structures, as mentioned, and only focus on the connection patterns). The three topologies are illustrated in Figure 12 (a),(b),(g),(m), and (n), Figure 12 (d), and (k), and Figure 12 (c),(e),(f),(h),(i),(j), and (l), respectively. Unless two $\mathcal{N}$s are pointing in opposite directions, and thus always attracting (namely the second scenario in Figure 12 (f)-(i)), all the scenarios can be mapped to the three topologies. The difference from the case with three modules is that when there are multiple destination modules to which the switched module can connect, the transitions can take multiple paths, and thus the process could be formulated in a probabilistic manner (such transitions are shown in dotted arrows). This type of probabilistic transition can be avoided if only one $\mathcal{N}$ is used, as shown in 12 (j)-(n), or by choosing deterministic transition paths (e.g. following the path from Figure 12 (d)→12 (a)→12 (b)→12 (e), instead of 12 (d)→12 (e), if the targeted configuration is 12 (e) and not 12 (c)).

To roughly verify the soundness of this assumption, we carried out an experiment with four modules, as originally presented in Figure 12 (a)-(e). We show the time series of one of the successful results in Figure 13. The demonstrated transitions are illustrated in Figure 12 (b) →12 (c) →12 (d) →12 (a) →12 (b). In some trials, as we show in the figure and Extension 2, the reconfiguration process runs quite smoothly, showing that the presented method is suited to reconfigurations with multiple modules. However, during other operations, we observed that the system often converged to an undesired formation, which was not exhibiting a connected structure or an energetically

global minimum state. That is, two identically oriented modules sometimes hindered a fourth module from approaching (Figure 12 (j); ideally, the expected topology is as shown in 12 (g). See Extension 2.). Considering that the effect of adhesion cannot be zero, as this hinders connected modules from regulating the relative angles through magnetic repulsions, this becomes a fundamental issue when there are more than four modules. The effect is partially studied as a local potential minimum (Miyashita et al. 2009), where magnetic potential acts as an "obstacle" for the assembly process. Further details are discussed in the next section.

[Insert Figure 13]

5.2 Influence of the Number of Neighbor Modules

Figure 14 (a)-(d) visualizes the system's potential energy U_{total} in a x-y space, describing with streamlines how an additional module, pointing in the same direction as the neighbor modules ($\uparrow$), would be attracted. Different types of configurations are respectively shown for cases in which a centered module has two neighbor modules (Figure 14 (a)), has three modules (Figure 14 (b)), four modules (Figure 14 (c)), or three modules, but with two featuring weak magnetization (Figure 14 (d)). For simplification, we use the same magnetic moment ($m = m_{NdFeB} = 2.63 \cdot 10^{-7}\,\mathrm{Am}^2$) and module mass ($w = w_{NdFeB} = 5.62 \cdot 10^{-8}\,\mathrm{kg}$). Figure 14 (b) implies that when the center module already has three neighborhoods, it can no longer attract another module (note our premise that neighbor modules keep a maximum distance, repelling each other). This tendency can also be seen in Figure 14 (c), where four modules surround a center module. As indicated with yellow arrows, the formation creates four local minimum positions in the space, spatially apart from the center module, hindering an additional module from getting closer to the center module.

[Insert Figure 14]

Incidentally, our system possesses the capability of regulating the strength of magnetization, which can be exploited to deal with this issue; namely, reducing the strength of magnetization for the Fe module by applying weak H_{act}. Suppose the case with three neighborhood cases (Figure 14 (b) and 14 (d)), where only two of the three neighbor modules are made of Fe, as in Figure 14 (b). When an external magnetic field H_{act} is strong enough to magnetize Fe modules, the cluster acts as one monopole, forming three local minimums in the space (14 (b)). In contrast, by weakening the strength of H_{act} to one fourth (0.4 is an arbitrary number), an attractive region is yielded, as indicated by the yellow arrow in 14 (d) ($\boldsymbol{m_{Fe}}$ becomes approximately one third under this H_{act}). This expansion and contraction of the attractive regions not only suggests that we can avoid the *magnetic potential wall* problem by adjusting the strength of H_{act} on occasion, but also that there is a possibility to use this characteristic for an advanced manipulation task in future work.

In addition to these discussions on the influence of the number of neighbor modules, structural stability should also be considered from the perspective of magnetism. The values (U_{mag}) shown

in Figure 14 (a)-(c) denote the magnetic potential energies of respective configurations; roughly speaking, given that modules are allowed to move freely in the space (ignoring the liquid surface curvature). The negative value of U_{mag} indicates that the formation is "stable", whereas a positive value indicates the formation is "unstable", and therefore the configuration tends to be decomposed (consider that if modules exist infinitely apart, the system's magnetic energy is zero). As shown, the magnetic potential energy of each configuration, with two neighbors, three neighbors, and four neighbors, is $-3.07{\cdot}10^{-11}$ J, $-3.97{\cdot}10^{-11}$ J, and $-3.83{\cdot}10^{-11}$ J, respectively, showing that the three-neighbor configuration is the most preferable. Moreover, when there are five neighbor modules, U_{mag} becomes $-1.96 \cdot 10^{-11}$ J, which still keeps a negative value, but once six modules surround a center module, which is the maximum number in this geometry, U_{mag} becomes $1.89 \cdot 10^{-11}$ J (> 0), implying that the structure is no longer configured intrinsically. With six neighbor modules, there also appears to be contact between two identically oriented modules, which in most cases is not ideal. Considering the results above, our premise is that up to five modules can have contact with the same module.

5.3 Generalization to N Module Transitions

This section investigates possible transition patterns with N modules, aiming to elucidate the relation between the numbers and the types of switchable modules that can maximize the representable topological patterns, when the number of modules (N) is given. To simplify the problem, we consider cases with five modules ($N = 5$). Figure 15 (a) shows all the possible configurations that can be represented with one switchable module (left-most column, when $k = 1$, $l = 1$), two switchable modules (middle column, $k = 2$, $l = 1$), three switchable modules (right middle, $k = 3$, $l = 1$), four switchable modules (right bottom, $k = 4$, $l = 1$), and five switchable modules (right-most bottom, $k = 5$, $l = 1$). The nodes represent modules and the links represent connections. The nodes representing switchable modules are highlighted with red dotted circles. In our case, assuming the case with N modules, the destination node(s) can be detected $2S$ steps away from the switching node ($S \in \mathbb{N}$, as colored orange in Figure 15 (a) with $N = 5$ case). If a switched module(s) is initially positioned at a terminal node(s), the transition does not break the topology of the rest of the group, and the realizable pattern is equal to the number of destination nodes. When such a module is positioned at a non-terminal node, a transition separates the group into several groups (the number is equal to the number of links initially connected to the switched node), increasing the combinatorial patterns for transformation. From the study above, we allow up to four links for the connection (five or six links connected to one node should also be geometrically allowed, but this only occurs with more than six modules). Since a link connects two modules that are pointing in opposite directions ($\mathcal{M}_i(\uparrow)$–$\mathcal{M}_j(\downarrow)$), the modules' orientation patterns are consequently constrained.

[Insert Figure 15]

We classify each configuration by tagging it with the topology-type (Y, I, T, or Z), the number of types of independently switchable modules (l), and the alphabetic ID, such as Y1a, Y1b, or I2a. We show the destination node(s) of a switched (transitioning) module in orange, together with the

configuration types, written in red font, which the group will transform into. Consider the case of Y1a, for example, in which we switch the magnetization of the top-left node (the highlighted node): the node gets detached from the group, and will reconnect to one of the nodes colored in orange. When the switched node lands on the orange node in the top right, the whole configuration transforms into I1a. If it connects to the orange node that is second from the bottom, the group transforms to Y1a; namely, it configures to an identical type of configuration.

We visualize all the transformable paths in Figure 15 (b), keeping the relative positions of configurations shown above in 15 (a). We again display deterministic transitions in solid arrows and probabilistic transitions in dotted arrows. It is important to note that none of the cases (from $k = 1$ to $k = 5$, at $l = 1$) can represent four distinctive topologies (namely Y, I, T, and Z) on its own; a group of T1b-Z1a is isolated from the rest of the connections in the case with $k = 1$, and the same phenomenon can also be found in the other cases. This means that representing four topologies with a single type of switchable module is impossible; a group may need to consist of several types of switchable modules ($l > 1$). Also, it can be seen that while there are some hub nodes that the system preferably transits, e.g. T1a or T2a, some configurations are not reachable from other configurations, such as Y1b, Y1c, I1b, and Y2b. Some topologies can be deterministically reached from other topologies with arbitrary initial configurations (i.e. T1a, Y1d, T1b, Z1a, T2a, Z2a, T3a, Z3a, and Y5a), while other topologies can only be reached probabilistically (i.e. Y1a, I1a, I1c, Y2a, Y2c, I2b, I2c, Y3a, and I3a). Potentially, each transition probability can theoretically be derived, though they fully depend on their transition history.

[Insert Figure 16]

The red, green, blue, and brown lines displayed in Figure 16, overlaid on the transition links shown in Figure 15, visualize the compatibility of all the different configurations with the same topology that can coexist (termed *coexisting link* hereafter). For example, a red link connecting Y1a and Y1b implies that there can be a configuration which has Y-topology, whose top-left module is a switchable module (e.g. $\mathcal{F}$), while the middle-top module is another type of switchable module (e.g. $\mathcal{A}$). This configuration enables a transition from Y-topology to T-topology (Y1b–T1a), though it still possesses the capability of transitioning from Y-topology to I-topology (Y1a–I1a) (please refer to Figure 15 (b) for a simple drawing). There are recursive links that come back to the same nodes, e.g. Y1a, I1a, T1a, Z1a. However, this coexistence does not help to increase the representable patterns.

By focusing on the isolation of link connections, it can be noticed that one of the easiest ways to conjugate two isolated groups and exhibit four different topologies is by linking T1a and T1b; that is, to arrange five modules in T-topology, use one switchable module for the terminal node (a node on the edge, e.g. $\mathcal{F}$) and use another type of switchable module for the non-terminal node (a node not on the edge, e.g. $\mathcal{A}$). Recognizing that the transformational path from I1b to T1a is one-directional, one scenario that exhibits all the topologies is to arrange I1b as the initial configuration (I-topology), transforming it to T1a (T-topology), then to Y1d (Y-topology), then coming back to T1a, and then to Z1a (Z-topology) via T1b (I1b →T1a →Y1d →T1a–T1b →Z1a). It should be noted that the four topologies are representable only when starting from I1b because of the

one-directional transition from I1b to T1a. Also, when transforming from T1a to Y1d, the other switchable module comes to stay at the orange node in the Y1d configuration, though this kind of information is not shown in the transition chart to avoid combinatorial divergence (to visualize this, one has to derive possible patterns for all the combinations shown in Figure 16). The chart shows the types of paths that exist, but it does not mention those that do not exist.

Let us focus on the blue *coexisting link* that connects T1b and T2a in Figure 16. The configuration formed by realizing this link is a T-topology, where one switchable module composes the center (e.g. $\mathcal{F}$) and two other switchable modules compose the different terminal nodes (e.g. $\mathcal{A}$). In this way, although the transitions are not perfectly deterministic, the configuration can be switched as: T2a →Y2a →T2a →I2c →T2a–T1b →Z1a, and all the topologies (Y, I, T, and Z) can be represented irrespective of the initial configuration. Figure 16 leads to the conclusion that given conditions $N = 5$ and $k = 1$, $l \geq 2$ is required in order to represent four topologies. This holds when $k = 2$ and $k = 3$. However, when $k = 4$ and $k = 5$, the system loses the capability to represent the four topologies regardless of l.

In general, with distinguishable N modules, there exist $(N-1)!+1$ patterns of node connections (the last +1 indicates when all are repelling). By incorporating physical rules, such as constraints coming from magnetic properties (e.g. only oppositely oriented modules can have a connection, or two separate groups cannot exist when $N > 3$, except when they all repel), the representable number of configurations decreases depending on the orientation of the modules. Moreover, in our case, because we do not distinguish the same type of modules, and we do not care the rotational order of connections to the same module, the number further decreases. Generalizing the relation between N, k, and l requires complete (or at least statistical) topological information about the group.

It can be expected that the controllability of the system increases along with less k and more l. Envisaged transitions with large N ($N \gg 1$) modules are illustrated in Figure 17; a case with different types of modules randomly mixed in 17 (a); and a case with few $\mathcal{F}$ or $\mathcal{A}$ in 17 (b). The scenarios with large numbers of modules are expected to have less unique formation patterns than those with four or five modules. As the illustration in Figure 17 (a) shows, the system should lose its controllability, and thus form randomly connected (or lattice-like) structures. Adopting many different types of magnets with separate magnetic coercivities will help, to some degree, but this cannot be the conclusive solution for addressability. A large difference in the modules' mixture ratios should cause "clustering", as highlighted with a dotted circle in Figure 17 (b). In the example, a small number of switchable magnets ($\mathcal{F}/\mathcal{A}$) are premixed with a large number of high coercivity magnets ($\mathcal{N}$). Flipping the polarity of the magnetization causes the attraction of the surrounding major modules, which subsequently creates clusters. For future work, we think there are several approaches to finding a solution for controlling large N modules. One is to allow a module to carry more than two magnets, as this can increase the encoding capability, which enables the module to selectively dock with another targeted module.

[Insert Figure 17]

6 Conclusion

This study reports magnetic micro-module reconfiguration based on local inter-magnetic interactions. The selected approach features the coupling of a bottom-up self-assembly formulation and a top-down feed-forward control, which facilitates the configuration of modules with a one-directional magnetic field. We first constrained the magnet orientation on a two-dimensional plane, such that they laterally interact, and thus their distances simply reflect the magnitude of interaction. We exploited the properties of magnetic materials as a solution to module addressability. The difference in coercivities among modules is exploited, such that a specific type of magnetic module is guided to reconfigure with the application of a material-dependent magnetic field. We investigated the properties by performing the magnetic attachment and detachment of two modules. For a proof-of-concept, we conducted reconfiguration experiments with three modules, and limited control over a four-module set. The experiments validated the reliability of reconfiguration with an increased number of modules. We further discussed cases with more than five modules, and the influence of neighboring modules on assembly processes, as this often hinders attracting modules. Given that the employed magnetic fields are along a single direction, there is promise for advancement to more complex morphologies with the inclusion of additional degrees of freedom. We emphasize that this contribution is the first experimental achievement of a magnetic micro-assembly system based on inter-modular interactions, providing a step forward in the development of a framework that fulfills the elemental prerequisites in the realization of magnet-based reconfigurable micro-systems.

Acknowledgments

This work was partially supported by Swiss National Science Foundation Fellowship PBZHP2-133472.

Appendix A: Index to Multimedia Extensions

The multimedia extension to this article is at: `http://www.ijrr.org`.

Extension	Media Type	Description
1	Video	Reconfiguration process with three modules ($\mathcal{A}$, $\mathcal{F}$, and $\mathcal{N}$) shown in Figure 11 (a)-(u). Five states shown in Figure 4 are represented in series.
2	Video	Successful reconfiguration processes with four modules ($\mathcal{F} \times 2$, $\mathcal{A} \times 1$, and $\mathcal{N} \times 1$) shown Figure 13 (a)-(i), followed by a failure trial seen in Figure 13 (j).

Appendix B: Module Fabrication

The modules were fabricated according to the following steps (ref. Figure 18). (a),(b) SU-8 was spin coated onto a silicon wafer to the desired thickness for the components. (c),(d) A mask pattern, which was previously designed with computer-aided design software, was patterned with UV light and hardened to create the positive mold. (e) Silicon rubber binding mix (Dow Corning,

HS II RTV) was poured into the positive mold and allowed to cure. (f) The silicon rubber was removed from the positive mold, creating the negative mold, which was the template of a core and a shell. (h),(i) A mixture of magnetic-powder-impregnated polyurethane (BJB Enterprise, TC-892) mold-making material was prepared by mixing four parts NdFeB powder to one part polyurethane, degassed in a vacuum, and then poured into a negative mold, which was previously designed for the core shape using the same process as (a)-(f). The alnico core and Fe core were cut, with the laser micro-mill (New Wave, QuickLaze-50ST), from their material pieces in order to maintain high magnetic permeabilities. (g),(j) A flat punch was pressed and held against the mold, which pushed out the excess material (polyurethane in (g), and NdFeB-polyurethane binding mix in (j)), leaving a thin backing layer. (k),(l) After hardening and removing the punch, each component was manually glued using resin (LOCTITE 416 Super Bonder) and a module was configured.

[Insert Figure 18]

Appendix C: Supporting Information of Surface Design

Figure 7 was taken from the top view to show the visual image of modules' side view. The composition is shown in Figure 19. We show a side view of a floating module in Figure 20 for a proof of small deformation of surface terrain caused by the module's weight.

[Insert Figure 19]

[Insert Figure 20]

References

Bishop, K. J. M., Wilmer, C. E., Soh, S., and Grzybowski, B. A. (2009). Nanoscale forces and their uses in self-assembly. *small*, **5**: 1600–1630.

Böhringer, K.-F., Goldberg, K., Cohn, M., Howe, R., and Pisano, A. (1998). Parallel microassembly with electrostatic force fields. In *IEEE International Conference on Robotics and Automation (ICRA)*, volume 2, pp. 1204–1211.

Boncheva, M., Ferrigno, R., Bruzewicz, D. A., and Whitesides, G. M. (2003). Plasticity in self-assembly: Templating generates functionally different circuits from a single precursor. *Angewandte Chemie International Edition*, **42**: 3368–3371.

Bowden, N., Choi, I. S., Grzybowski, B. A., and Whitesides, G. M. (1999). Mesoscale self-assembly of hexagonal plates using lateral capillary forces: Synthesis using the capillary bond. *Journal of American Chemical Society*, **121**: 5373–5391.

Braillon, P. M. (1978). Magnetic plate comprising permanent magnets and electropermanent magnets.

Cohn, M. B. and Kim, C.-J. (1991). Self-assembling electrical networks: An application of micromachining technology. In *International Conference on Solid-State Sensors and Actuators*, pp. 490–493.

Dejeu, J., Rougeot, P., Gauthier, M., and Boireau, W. (2009). Robotic submerged microhandling controlled by pH switching. In *IEEE/RSJ International Conference on Intelligent Robots and Systems (IROS)*, pp. 1855–1860.

Demaine, E. D., Hohenberger, S., and Liben-Nowell, D. (2002). Tetris is hard, even to approximate. Technical report, Cornell University Library arXiv.org.

Diller, E., Floyd, S., Pawashe, C., and Sitti, M. (2011). Control of multiple heterogeneous magnetic micro-robots in two dimensions. *IEEE Transactions on Robotics*, p. DOI: 10.1109/TRO.2011.2170330.

Diller, E., Miyashita, S., and Sitti, M. (2012a). Magnetic hysteresis for multi-state addressable magnetic microrobotic contro. In *Int. Conf. on Intelligent Robots and Systems*, pp. 2325–2331.

Diller, E., Miyashita, S., and Sitti, M. (2012b). Remotely addressable magnetic composite micropumps. *RSC Advances*, **2**(9): 3850 – 3856. DOI: 10.1039/C2RA01318E.

Donald, B. R., Levey, C. G., McGray, C. D., Paprotny, I., and Rus, D. (2006). An untethered, electrostatic, globally controllable MEMS micro-robot. *Journal of microelectromechanical systems*, **15**: 1–15.

Donald, B. R., Levey, C. G., and Paprotny, I. (2008). Planar microassembly by parallel actuation of MEMS microrobots. *Journal of microelectromechanical systems*, **17**: 789–808.

Edgar, R. F., Martzloff, F. D., and Tompkins, R. E. (1972). Magnetic latch and switch using cobalt-rare earth permanent magnets.

Feiner, A., Lovell, C. A., Lowry, T. N., and Ridinger, P. G. (1960). The ferreed - a new switching device. *The Bell System Technical Journal*, **39**: 1–30.

Floyd, S., Pawashe, C., and Sitti, M. (2009a). Microparticle manipulation using multiple untethered magnetic micro-robots on an electrostatic surface. In *IEEE/RSJ International Conference on Intelligent Robots and Systems (IROS)*, pp. 528–533.

Floyd, S., Pawashe, C., and Sitti, M. (2009b). Modeling and experimental characterization of an untethered magnetic micro-robot. *The International Journal of Robotics Research*, **28**: 1077–1094.

Frutiger, D. R., Vollmers, K., Kratochvil, B. E., and Nelson, B. J. (2009). Small, fast, and under control: wireless resonant magnetic micro-agents. *International Journal of Robotics Research*, **13**: 1–24.

Gendreau, D., Gauthier, M., Heriban, D., and Lutz, P. (2010). Modular architecture of the microfactories for automatic micro-assembly. *Robotics and Computer-Integrated Manufacturing*, **26**: 354–360.

Gilpin, K., Knaian, A., and Rus, D. (2010). Robot pebbles: One centimeter module for programmable matter through self-disassembly. In *IEEE International Conference on Robotics and Automation (ICRA)*, pp. 2485 – 2492.

Gracias, D. H., Tien, J., Breen, T. L., Hsu, C., and Whitesides, G. M. (2000). Forming electrical networks in three dimensions by self-assembly. *Science*, **289**(5482): 1170–1172.

Grzybowski, B. A., Winkleman, A., Wiles, J. A., Brumer, Y., and Whitesides, G. M. (2003). Electrostatic self-assembly of macroscopic crystals using contact electrification. *Nature Materials*, **2**: 241–245.

Grzybowski, B. A., Radkowski, M., Campbell, C. J., Lee, J. N., and Whitesides, G. M. (2004). Self-assembling fluidic machines. *Applied physics letters*, **84**: 1798–1800.

Hosokawa, K., Shimoyama, I., and Miura, H. (1996). Two-dimensional micro-self-assembly using the surface tension of water. *Sensors and Actuators A*, **57**: 117–125.

Israelson, A. F. (1969). Turn-off permanent magnet.

Jacobs, H. O., Tao, A. R., Schwartz, A., Gracias, D. H., and Whitesides, G. M. (2002). Fabrication of a cylindrical display by patterned assembly. *Science*, **296**: 323–325.

Karagozler, M. E., Campbell, J. D., Fedder, G. K., Goldstein, S. C., Weller, M. P., and Yoon, B. W. (2007). Electrostatic latching for inter-module adhesion, power transfer, and communication in modular robots. In *IEEE International Conference on Intelligent Robots and Systems (IROS)*, pp. 2779–2786.

Klavins, E. (2007). Programmable self-assembly. *IEEE Control System Magazine*, **27**: 43–56.

Kummer, M. P., Abbott, J. J., Kratochvil, B. E., Borer, R., Sengul, A., and Nelson, B. J. (2010). Octomag: An electromagnetic system for 5-dof wireless micromanipulation. In *IEEE International Conference on Robotics and Automation (ICRA)*, pp. 1006–1017.

Love, J. C., Urbach, A. R., Prentiss, M. G., and Whitesides, G. M. (2003). Three-dimensional self-assembly of metallic rods with submicron diameters using magnetic interactions. *Journal of American Chemical Society*, **125**: 12696–12697.

Mao, C., Thalladi, V. R., Wolfe, D. B., Whitesides, S., and Whitesides, G. M. (2002). Dissections: Self-assembled aggregates that spontaneously reconfigure their structures when their environment changes. *Journal of the American Chemical Society*, **124**(49): 14508 –14509.

Mastrangeli, M., Abbasi, S., Varel, C., Hoof, C. V., Celis, J.-P., and B ohringer, K. F. (2009). Self-assembly from milli- to nanoscales: methods and applications. *Journal of Micromechanics and Microengineering*, **19**: 1–37.

Mermoud, G., Mastrangeli, M., Upadhyay, U., and Martinoli, A. (2012). Real-time automated modeling and control of self-assembling systems. In *IEEE International Conference on Robotics and Automation*.

Miyashita, S., Casanova, F., Lungarella, M., and Rolf Pfeifer, F. (2008). Peltier-based freeze-thaw connector for waterborne self-assembly systems. In *IEEE/RSJ International Conference on Intelligent Robots and Systems (IROS)*, pp. 1325–1330.

Miyashita, S., Nagy, Z., Nelson, B. J., and Pfeifer, R. (2009). The influence of shape on parallel self-assembly. *Entropy*, **11**: 643–666.

Napp, N., Burden, S., and Klavins, E. (2006). The statistical dynamics of programmed self-assembly. In *IEEE International Conference on Robotics and Automation (ICRA)*, pp. 1469–1476.

Pawashe, C., Floyd, S., and Sitti, M. (2009). Magnetic microrobot control using electrostatic clamping. *Applied Physics Letters*, **94**: 164108.

Pelesko, J. A. (2007). *SELF ASSEMBLY*. Chapman & Hall/CRC.

Penrose, L. S. (1958). Mechanics of self-reproduction. *Annals of Human Genetics*, **23**: 59–72.

Pignataro, D. F. (2001). Electrically switchable magnet system.

Ramadan, Q., Uk, Y. S., and Vaidyanathan, K. (2007). Large scale microcomponents assembly using an external magnetic array. *Applied Physics Letters*, **90**: 172502–1.

Randhawa, J. S., Kanu, L. N., Singh, G., and Gracias, D. H. (2010). Importance of surface patterns for defect mitigation in three-dimensional self-assembly. *Langmuir*, **26**: 12534–12539.

Rochat, F., Schoeneich, P., Bonani, M., Magnenat, S., Mondada, F., and Bleuler, H. (2010). Design of magnetic switchable device (MSD) and applications in climbing robot. In *The 13th International Conference on Climbing and Walking Robots and the Support Technologies for Mobile Machines (CLAWAR)*, pp. 375–382.

Rothemund, P. W. K. (2000). Using lateral capillary forces to compute by self-assembly. *Proceedings of the National Academy of Sciences*, **97**: 984–989.

Saitou, K. (1999). Conformational switching in self-assembling mechanical systems. *IEEE Transactions on Robotics and Automation*, **15**: 510–520.

Saitou, K. and Jakiela, M. J. (1995). Subassembly generation via mechanical conformational switches. *Artificial Life*, **2**: 377–416.

Schempf, H., Chemel, B., and Everett, N. (1995). Neptune: Above-ground storage tank inspetion robot system. *IEEE Robotics & Automation, Society Magazine*, **2**: 9–15.

Shetye, S. B., Eskinazi, I., and Arnold, D. P. (2008). Self-assembly of millimeter-scale components using integrated micromagnets. *IEEE Transactions on Magnetics*, **44**: 4293–4296.

Sitti, M. (2009). Voyage of the microrobots. *Nature*, **458**: 1121–1122.

Tolley, M. T., Kalontarov, M., Neubert, J., Erikson, D., and Lipson, H. (2010). Stochastic modular robotic systems: A study of fluidic assembly strategies. *IEEE Transactions on Robotics*, **26**: 518–530.

White, P., Zykov, V., Bongard, J., and Lipson, H. (2005). Three dimensional stochastic reconfiguration of modular robots. In *International Conference on Robotics Science and Systems (RSS)*, pp. 161–168.

Whitesides, G. M. and Grzybowski, B. (2002). Self-assembly at all scales. *Science*, **295**: 2418–2421.

Wolfe, D. B., Snead, A., Mao, C., Bowden, N. B., and Whitesides, G. M. (2003). Mesoscale self-assembly: Capillary interactions when positive and negitive menisci have similar amplitudes. *Langmuir*, **19**(6): 2206–2214.

Yokoi, H., Nagai, T., Ishida, T., Fujii, M., and Iida, T. (2003). *Morpho-functional Machines: The New Species: Designing Embodied Intelligence*. Springer.

Zhou, Q. and Chang, B. (2006). Microhandling using robotic manipulation and capillary self-alignment. In *IEEE/RSJ International Conference on Intelligent Robots and Systems (IROS)*, pp. 5883–5888.

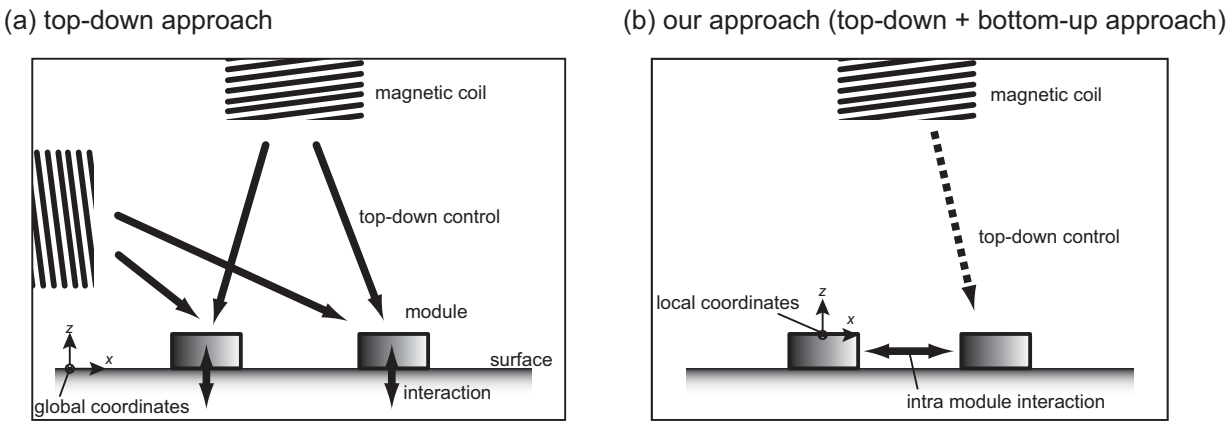

Figure 1: Differences in approaches for micro-assembly. (a) Typical top-down approach, where modules receive signals and act accordingly. (b) Our scope in this study is the combination of the bottom-up and top-down approaches. Note that the driving mechanism is module-module interaction, which is indirectly guided in the top-down manner.

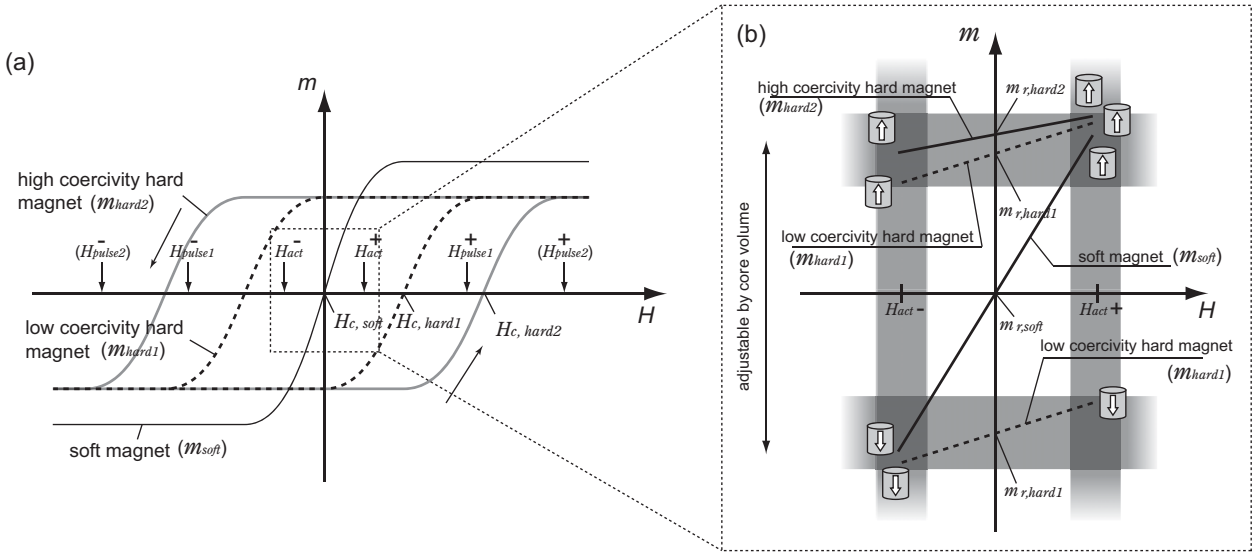

Figure 2: m-H curves of a soft magnet ($\boldsymbol{m_{soft}}$), a low coercivity hard magnet ($\boldsymbol{m_{hard1}}$), and a high coercivity hard magnet ($\boldsymbol{m_{hard2}}$). (a) $\boldsymbol{m_{soft}}$, with coercivity $H_{c,soft}$, switches its magnetization without hysteresis using H_{act}; $\boldsymbol{m_{hard1}}$, with coercivity $H^{\pm}_{c,hard1}$, switches with hysteresis, using a strong pulsing magnetic field (hereafter termed $H^{\pm}_{pulse}$); and $\boldsymbol{m_{hard2}}$, with coercivity $H^{\pm}_{c,hard2}$, keeps its magnetization, regardless of the applied fields. (b) m-H curves with a smaller sweep of H, where both hard magnets were pre-magnetized to show similar values of m. Both m_{hard1} and m_{hard2} keep their signs either, positive or negative, with respect to H, while m_{soft} changes the value from negative to positive.

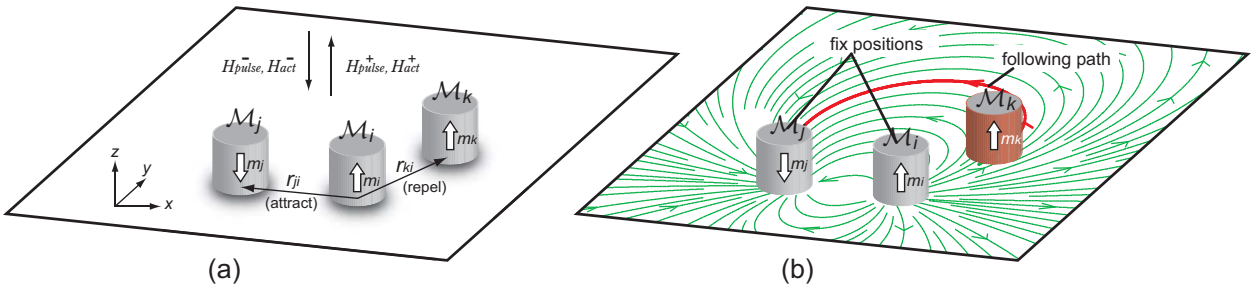

Figure 3: Three magnetic dipoles (i, j, and k) aligned in parallel on a 2D x-y-plane. (a) The attractive/repulsive force is determined by the orientation of the magnetic moments. (b) When the positions of $\mathcal{M}_i$ and $\mathcal{M}_j$ are fixed, $\mathcal{M}_k$ follows the path which is derived from U_{mag} (colored red).

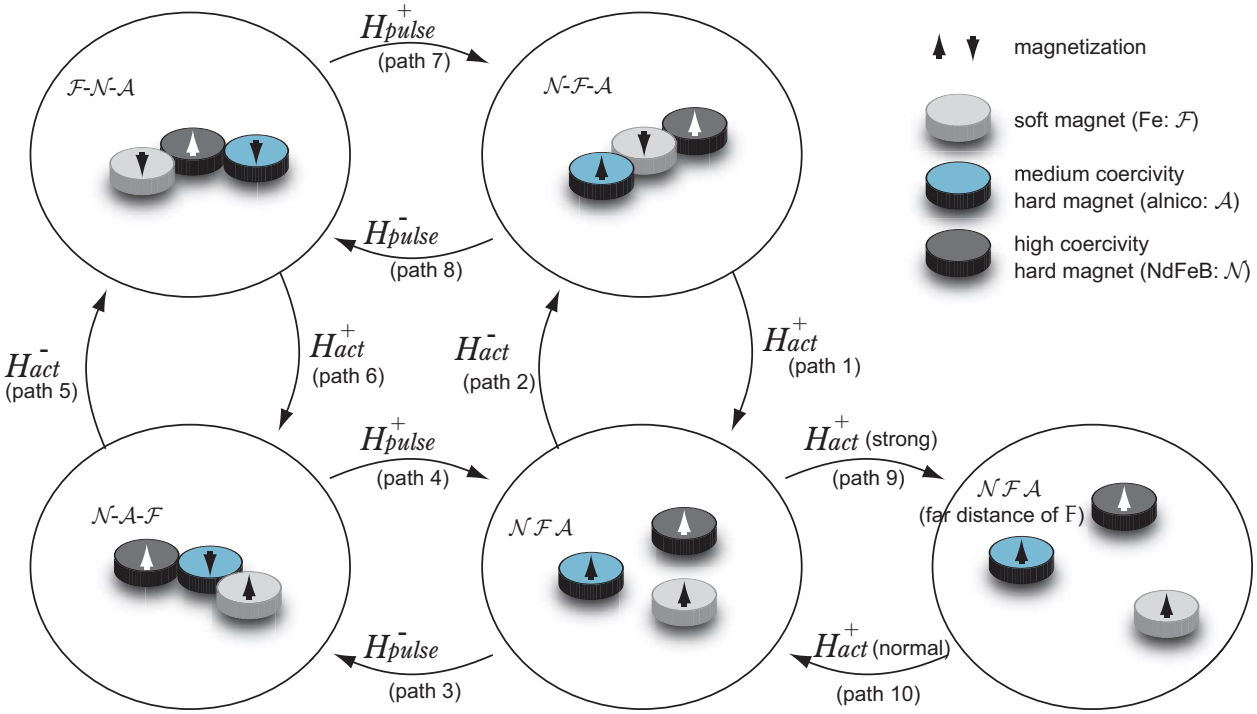

Figure 4: State transition diagram of five reversible configurations with three magnetic modules.

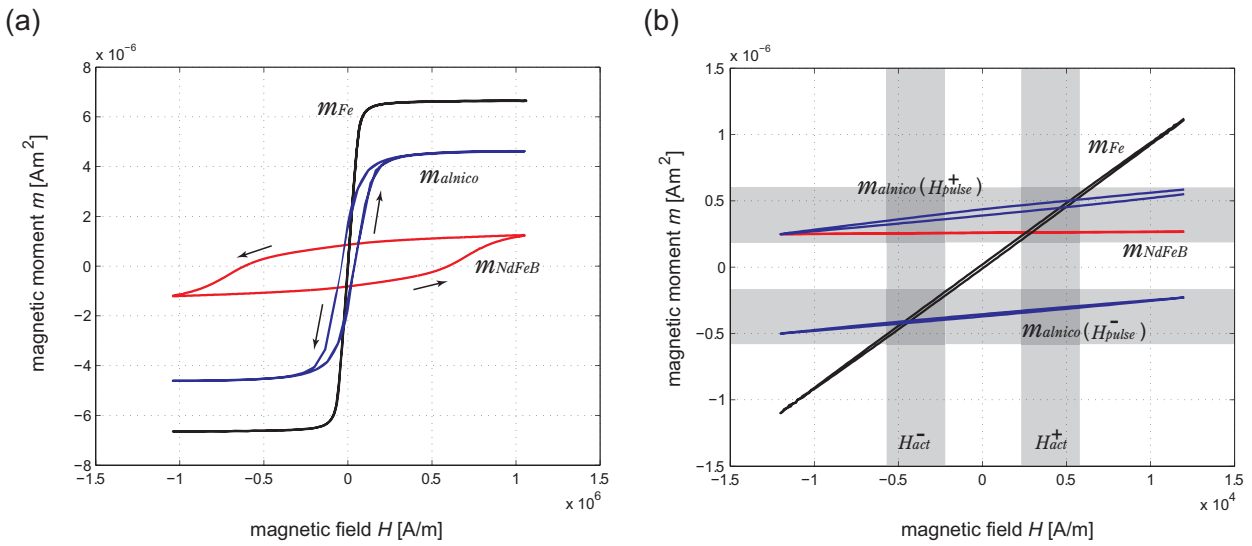

Figure 5: Experimental m-H loop of three magnetic materials, under the application of magnetic fields: (a) measured up to the AGFM machine's maximum performance (1.114×10^6 A/m), and (b) measured around the H_{act} region.

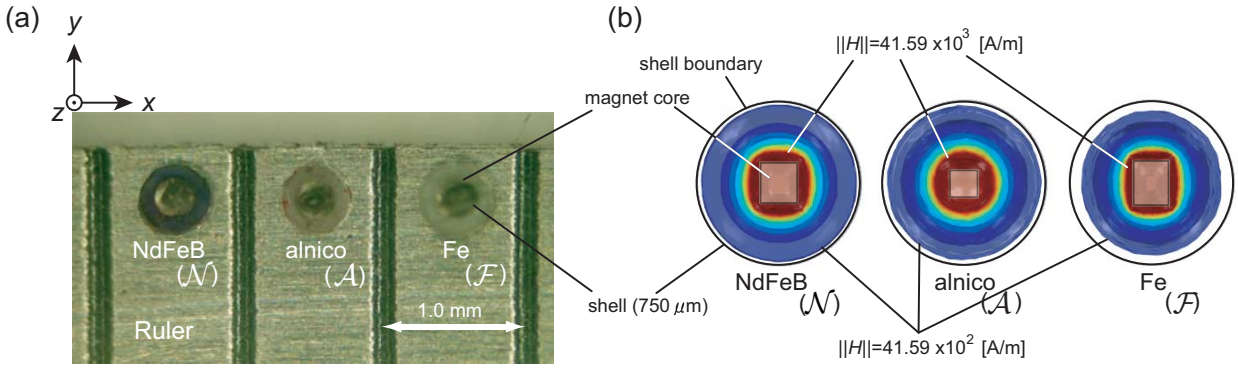

Figure 6: The designed magnetic micro-modules. (a) Three magnetic micro-modules ($\mathcal{N}$, $\mathcal{A}$, and $\mathcal{F}$) on a ruler from the top view. Magnets (termed "cores") are surrounded with polyurethane "shells". (b) Visualized magnetic field strength distributions created by each magnet, analyzed by a finite element method (obtained using COMSOL software).

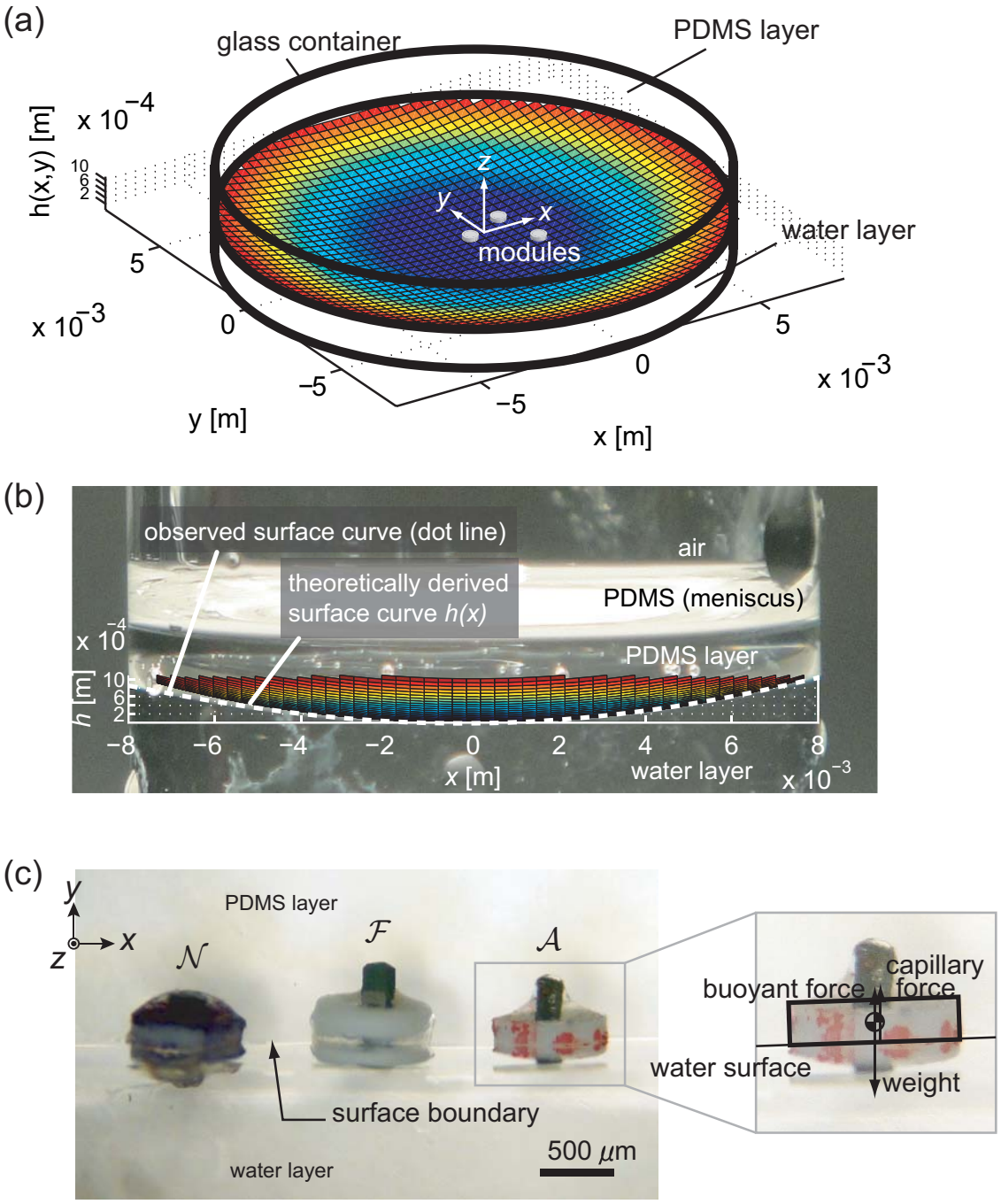

Figure 7: Liquid surface design. (a) Calculated water surface profile with module illustrations and (b) a comparison with the experimentally obtained surface curve from the side view. (c) Layers in which the module bodies are present. Modules are placed vertically with their sides facing up, and situated between two liquid layers (ref. Figure 19 for the composition, and see Figure 20 for a horizontal view of a floating module). Note that the body parts in the water layer are reflections.

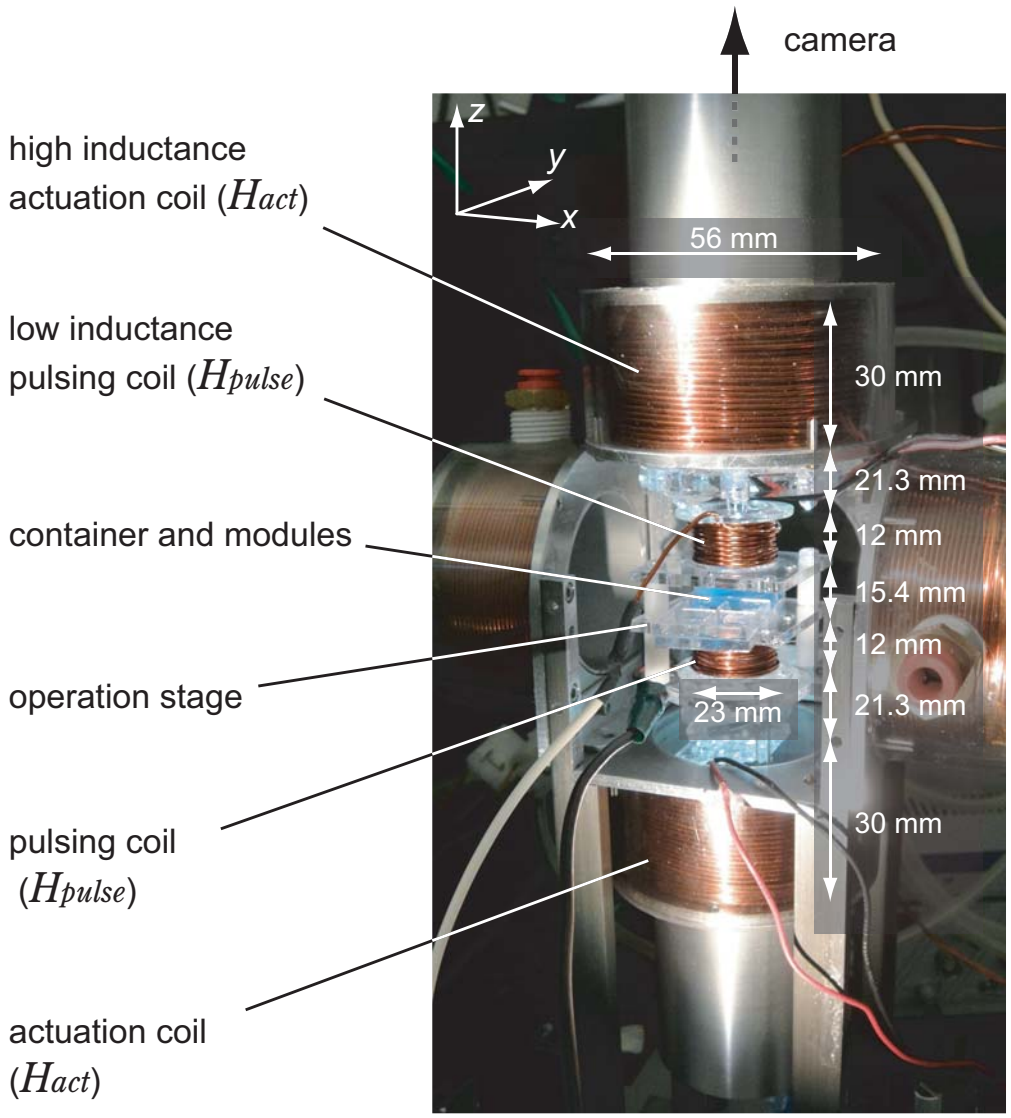

Figure 8: A schematic and a photograph of the coil system. The container is placed between a low inductance pulsing coil pair (H_{pulse}), which is further sandwiched by a high inductance actuation coil pair (H_{act}).

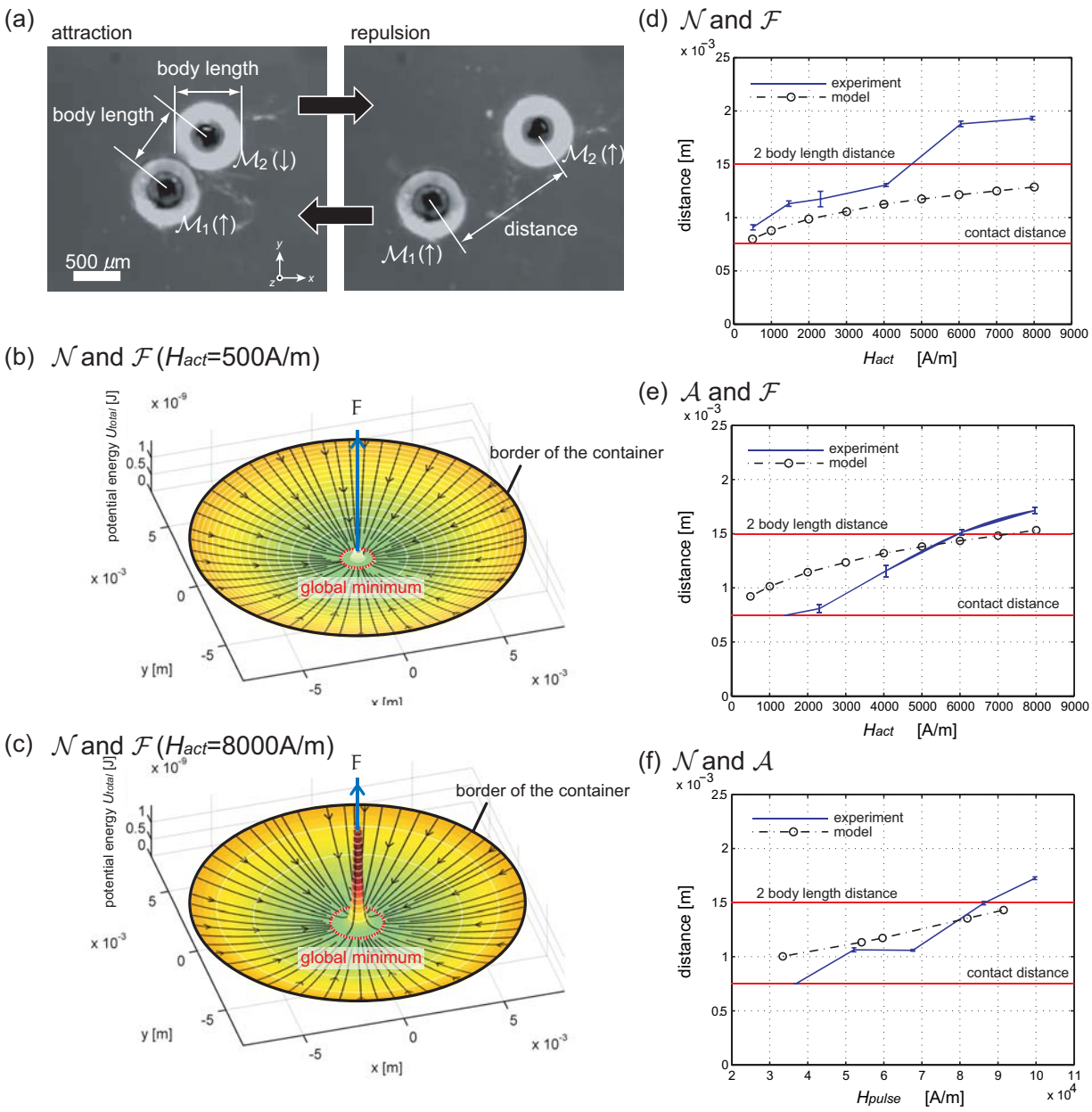

Figure 9: A reversible magnetic attraction/repulsion of micro-modules. (a) Snapshots from a trial. (b),(c) U_{total} of $\mathcal{N}, \mathcal{F}$ pair in x-y-space, placing $\mathcal{F}$ in the center; when applied H_{act} is 500 A/m (b) and when $H_{act} = 8000$ A/m (c). The contours are depicted every $0.05 \cdot 10^{-9}$ J. (d)-(f) Theoretical and experimental module distances, when applying different H_{act} (for $\mathcal{N}, \mathcal{F}$ pair in (d) and for $\mathcal{A}, \mathcal{F}$ pair in (e)), and when applying different H_{pulse} for $\mathcal{N}, \mathcal{A}$ pair (f).

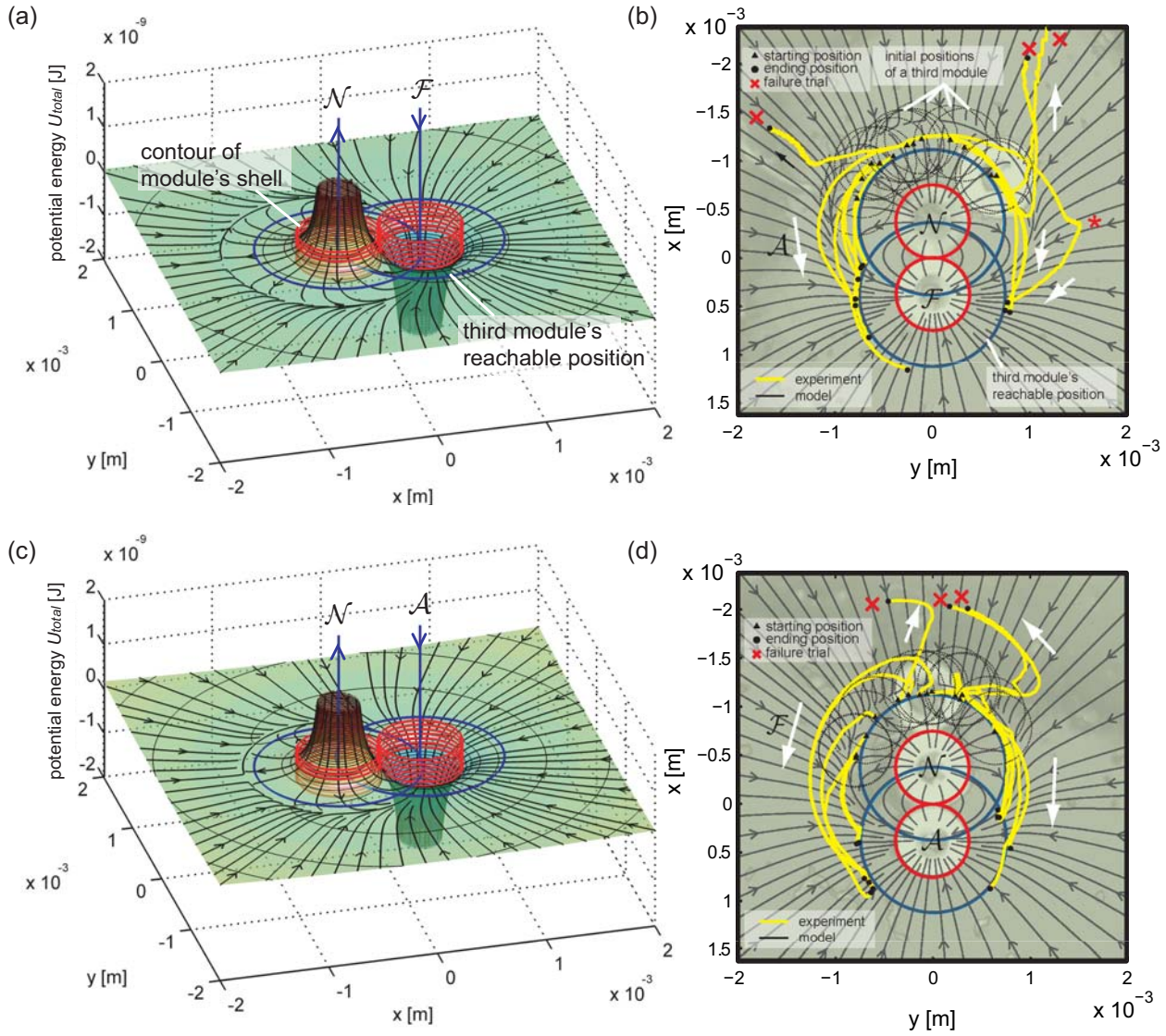

Figure 10: Potential energy curves U_{total} of three modules in x-y-space ((a) and (c)), and the experimentally obtained trajectories of a third module in local coordination when the magnetization is switched ((b) and (d)), with the $\mathcal{N}(\uparrow), \mathcal{F}(\downarrow)$ pair (in (a) and (b)) and the $\mathcal{N}(\uparrow), \mathcal{A}(\downarrow)$ pair (in (c) and (d)). We display the contours of module shells with red circles, and the third module's reachable position with blue circles. Note that in this case study, the center of the third module cannot reach inside the blue circles. In the right column, the estimated trajectories of translating modules are mapped as stream lines, together with the respective starting positions and ending positions, as indicated with triangles and circular dots. During the experiments, three assembly failures were observed in both cases (76.9 % success rate, marked as red "×" in the figure). An unintended motion, illustrated with the label $*$ in (b), is likely due to the influence of the asymmetric geometry of $\mathcal{F}$, which may cause a disturbed flux distribution.

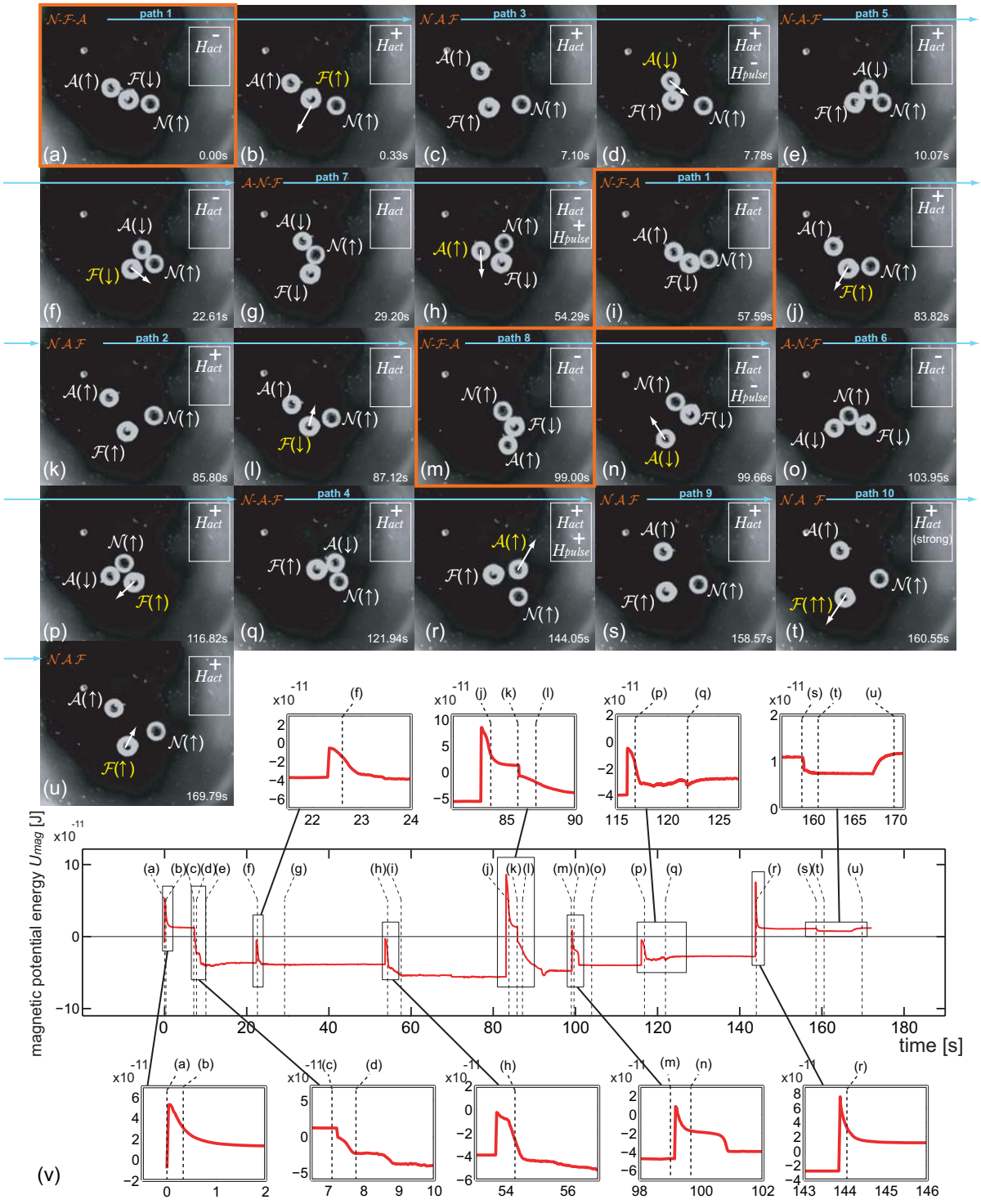

Figure 11: (a)-(u) Reconfiguration process with three magnetic micro-modules. All the transition paths, appearing in Figure 4 (path 1 to path 10) are performed (see Extension 1 for the movie). (v) Time evolution of the magnetic potential energy. Corresponding time periods to the snapshots are indicated with subscripts (a)-(u). The snapshots framed with orange windows show the same configurations as (a).

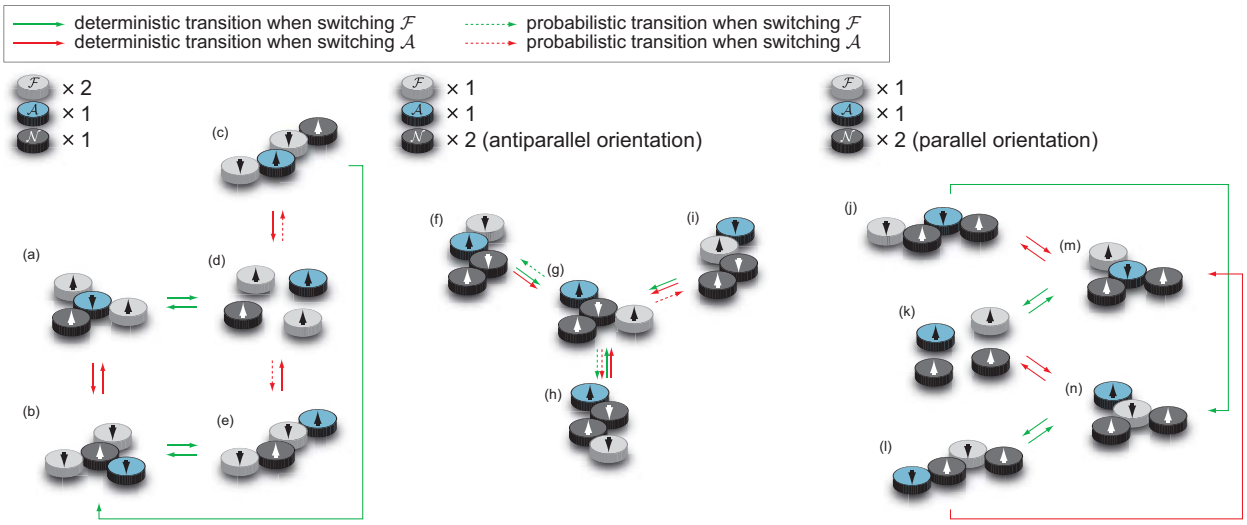

Figure 12: Cases with four modules. We count transitions that are reversible. Exceptions are shown in brackets, in which the pattern of the magnetizations are the same as the original configuration, but with more connections, and thus a more energetically stable state.

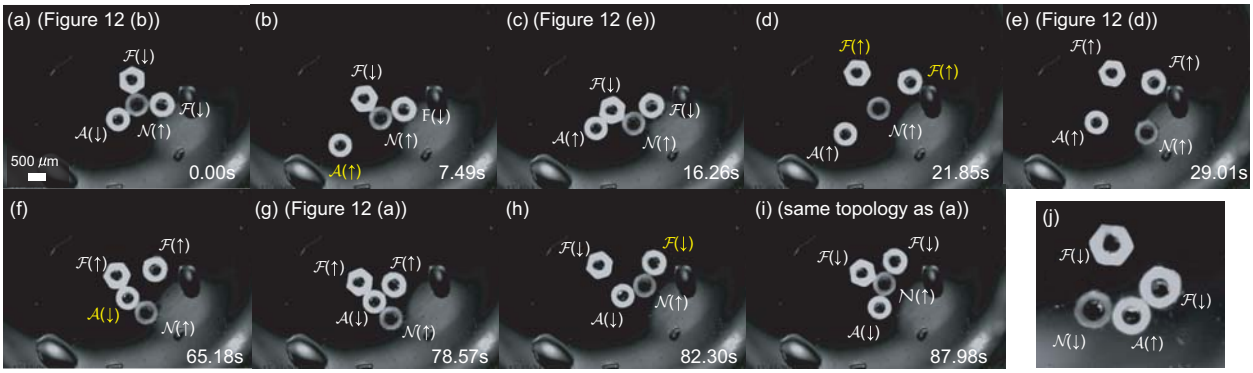

Figure 13: Snapshots of a trial with four modules. The demonstrated transitions are Figure 12 (b) ((a) in this figure) → 12 (e) ((c)) → 12 (d) ((e)) → 12 (a) ((g)) → 12 (b) ((i)). In trials, undesired formations that did not attain the energetically global minimum, as shown in (j), occurred frequently (see Extension 2).

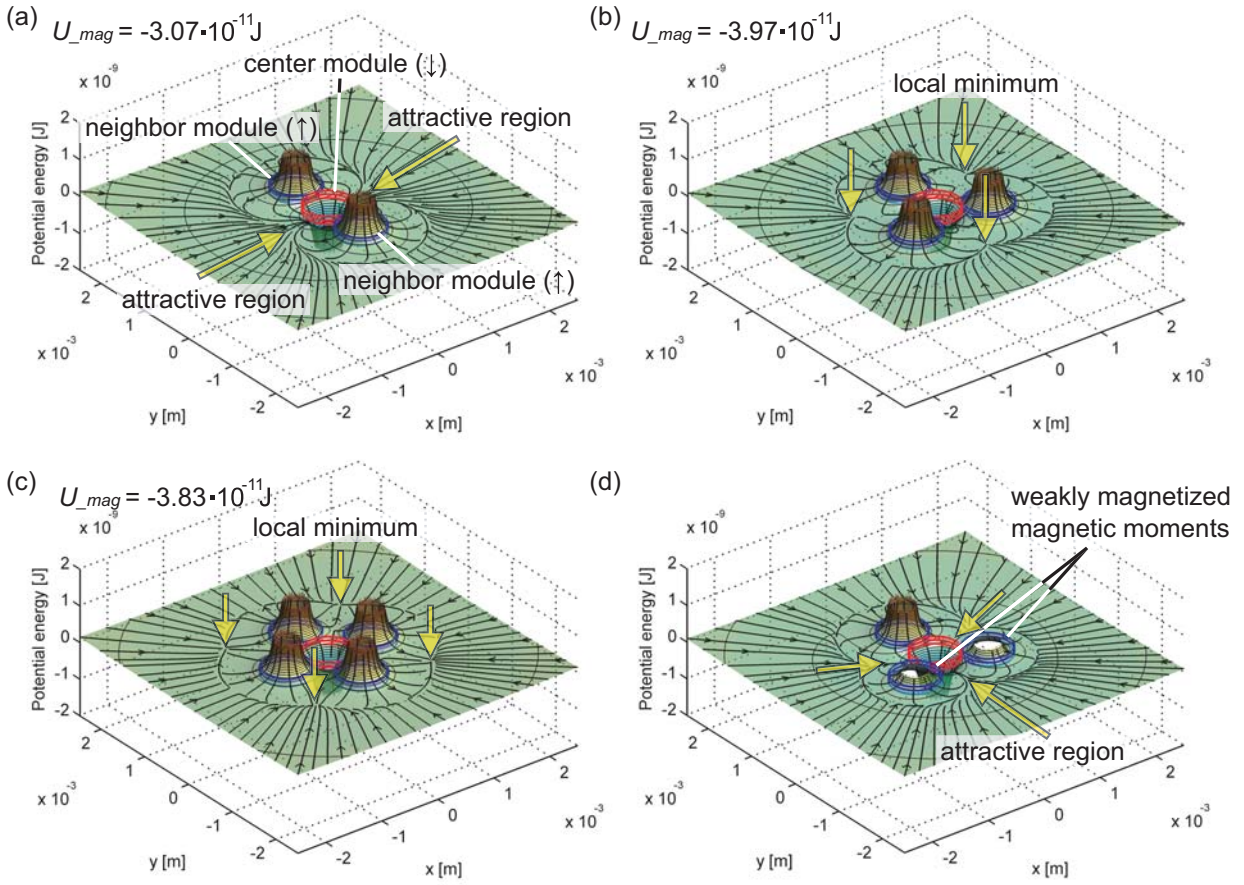

Figure 14: A system's potential energy U_{total} describing with streamlines how an additional module, pointing in the same direction as neighbor modules (↑), is attracted when a centered module has two neighbor modules (a), three modules (b), four modules (c), or three modules, but with two featuring weak magnetization (d). We assume all the magnets have the same magnetic moments, except the two in (d). Terrains are shown up to half the distance of the module radius, as usual.

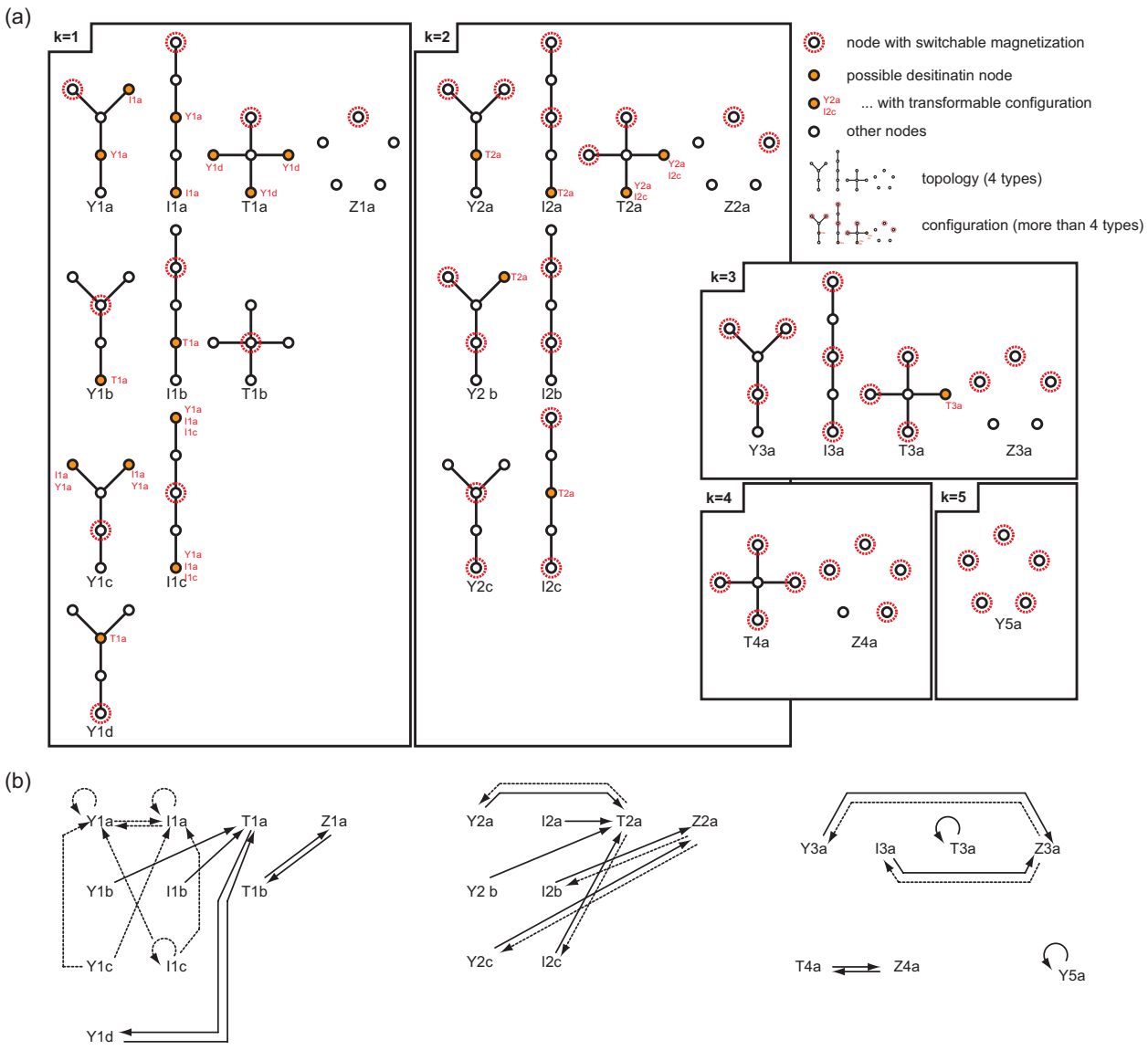

Figure 15: (a) Classification of configurations with five modules ($N = 5$), which contain: one switchable module (left-most column, when $k = 1$, $l = 1$), two switchable modules (middle column, $k = 2$, $l = 1$), three switchable modules (right middle, $k = 3$, $l = 1$), four switchable modules (right bottom, $k = 4$, $l = 1$), and five switchable modules (right-most bottom, $k = 5$, $l = 1$). The nodes represent modules and the links represent connections. The nodes representing switchable modules are highlighted with red circles. A possible destination node(s) of a switched (transitioning) module is colored in orange, together with the configuration type(s), written in red font, which the configuration will transform into. Each configuration is tagged with a combination of the topology-type (Y, I, T, or Z), the number of types of independently switchable modules (l), and the alphabetic ID (e.g. Y1a, Y1b, I2a). (b) The transformable paths of the configurations, keeping the relative positions of configurations shown in (a). Deterministic transitions are displayed in solid arrows and probabilistic transitions in dotted arrows.

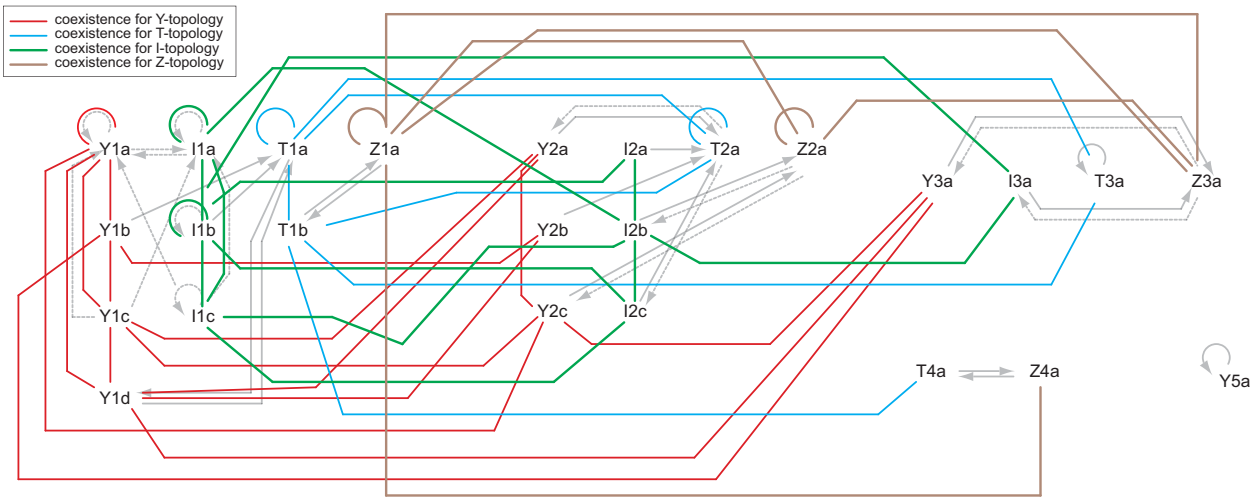

Figure 16: Compatibility of all the different configurations with the same topology that can coexist. The red, green, blue, and brown lines, overlaid on the transition links shown in Figure 15 (b), visualize the possibility of coexistence.

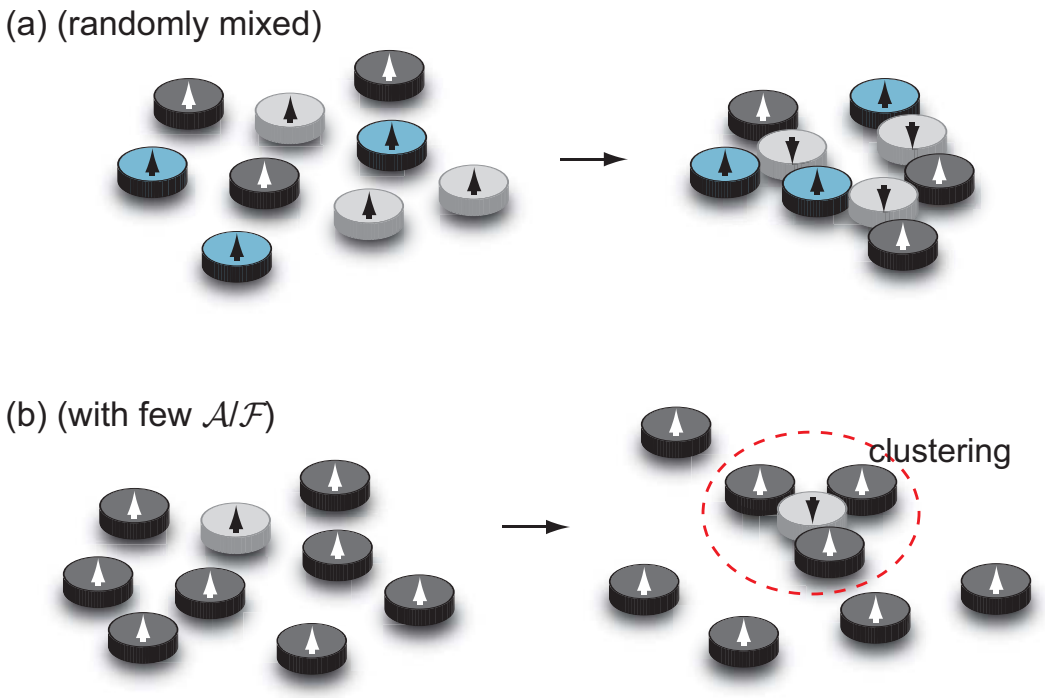

Figure 17: Transition patterns with N ($N \gg 1$) modules. (a) Different types of modules are randomly mixed. The system should lose its controllability, and thus form randomly connected lattice-like structures. (b) A case with few $\mathcal{F}$ or $\mathcal{A}$. The polarized mixing ratios should cause "clustering" (highlighted with a red dotted circle).

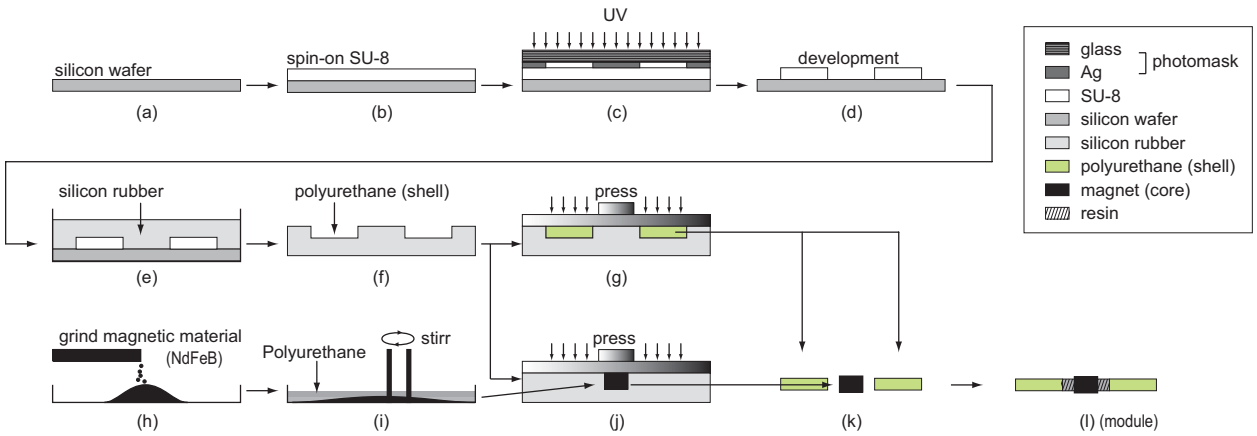

Figure 18: Fabrication process of a magnetic micro-module.

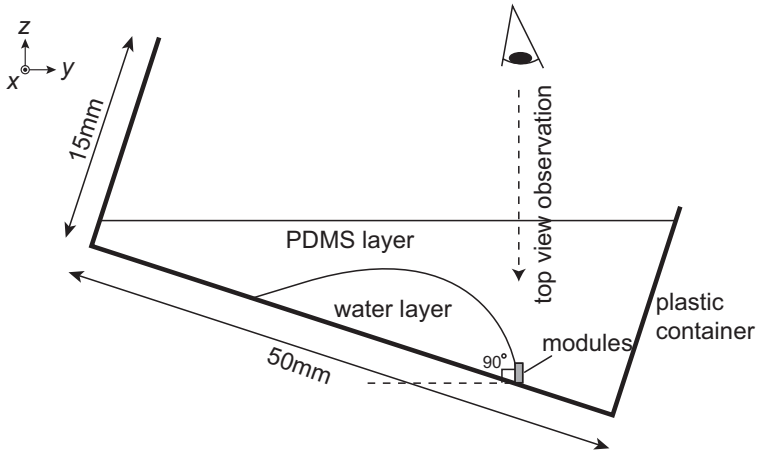

Figure 19: Composition of modules in Figure 7 (c). Modules are placed vertically with their sides facing up, and situated between two liquid layers. The two layers are formed in a tilted plastic container, where the water layer creates negative menisci, providing modules with a vertical surface on which to stand horizontally.

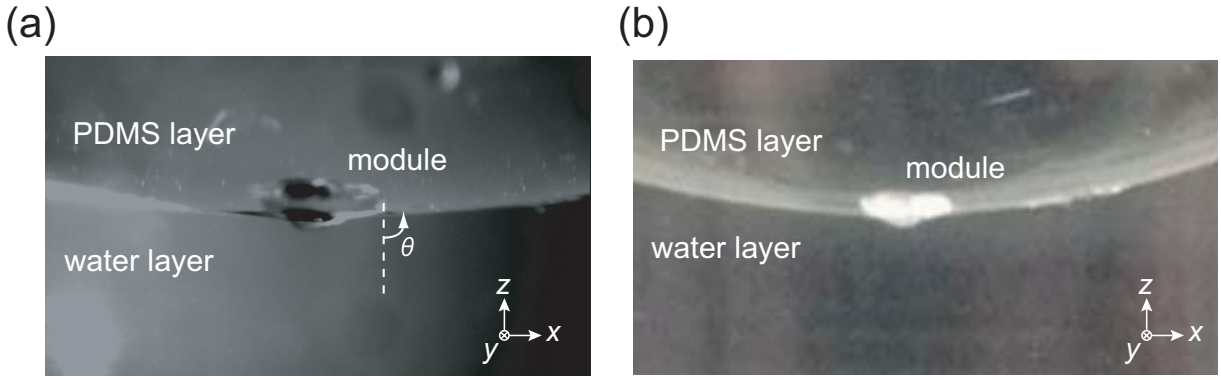

Figure 20: Horizontal view of the floating module ($\mathcal{F}$). The two pictures were taken under different light conditions. Little deformation of the surface caused by the module's weight is apparent. θ is the contact angle of the surface measured down from vertical axis.

Table 1: Magnetic micro-module properties.

	core					
	dimension $L \times W \times H$ [μm^3]	volume $\times 10^{-12}$ [m^3]	density [kg/m^3]	coercivity (H_c) [kA/m]	magnetic moment $\times 10^{-7}$[Am^2] under $H_{act}+$	under $H_{act}-$
Fe ($\mathcal{F}$)	$170 \times 220 \times 530$	19.82	7860	0.647	3.98	-3.46
alnico ($\mathcal{A}$)	$110 \times 110 \times 480$	5.81	7300	41.59	4.88 (-3.11^*)	3.77 (-4.00^*)
NdFeB ($\mathcal{N}$)	$180 \times 200 \times 300$	10.80	5313	605.90	2.63	2.56

	shell**			total (core + shell)		
	diameter $\times$ height $\phi \times H$ [μm^2]	volume $\times 10^{-12}$[m^3]	density [kg/m^3]	volume $\times 10^{-12}$[m^3]	mass $\times 10^{-7}$[kg]	mass counting buoyancy $\times 10^{-8}$[kg]
Fe ($\mathcal{F}$)	750×170	68.75	1140	88.57	2.34	14.5
alnico ($\mathcal{A}$)		73.05		78.86	1.26	4.71
NdFeB ($\mathcal{N}$)		69.00		79.80	1.36	5.62

* when applied $H_{pulse}-$

** The resin part was counted as a part of shell.